JM PAPERS

Phononic compliant surfaces for the suppression of travelling-wave flutter instabilities in boundary-layer flows

Nicolò Fabbiane[1] [ID], Olivier Marquet[2] [ID], Lorenzo Pierpaoli[1,3] [ID], Régis Cottereau[3] [ID] and Marie Couliou[2] [ID]

[1]DAAA, ONERA, Institut Polytechnique de Paris, 92320 Châtillon, France
[2]DAAA, ONERA, Institut Polytechnique de Paris, 92190 Meudon, France
[3]Aix-Marseille Université, CNRS, Centrale Méditerranée, LMA, 13453 Marseille, France
Corresponding author: Nicolò Fabbiane, nicolo.fabbiane@onera.fr

Compliant walls made from homogeneous viscoelastic materials may attenuate the amplification of Tollmien–Schlichting waves (TSWs) in a two-dimensional boundary-layer flow, but they also amplify travelling-wave flutter (TWF) instabilities at the interface between the fluid and the solid, which may lead to a premature laminar-to-turbulent transition. To mitigate the detrimental amplification of TWF, we propose to design compliant surfaces using phononic structures that aim at avoiding the propagation of elastic waves in the solid in the frequency range corresponding to the TWF. Thus, stiff inserts are periodically incorporated into the viscoelastic wall in order to create a band gap in the frequency spectrum of the purely solid modes. Fluid–structural resolvent analysis shows that a significant reduction in the amplification peak related to TWF is achieved while only marginal deterioration in the control of TSWs is observed. This observation suggests that the control of TSWs is still achieved by the overall compliance of the wall, while the periodic inserts inhibit the amplification of TWF. Bloch analysis is employed to discuss the propagation of elastic waves in the phononic surface to deduce design principles, accounting for the interaction with the flow.

Key words: flow-structure interactions, boundary layer stability, instability control

1. Introduction

The concept of employing compliant walls for passive control of boundary-layer instabilities has its roots in the mid-twentieth century, with the seminal works by Benjamin

(1960), Kramer (1961) and Landahl (1962). In this context, the primary objective is to mitigate the spatial growth of Tollmien–Schlichting waves (TSWs), a linear, convective instability of the boundary layer that, in low-disturbance environments, brings about the onset of the laminar-to-turbulent transition (Kachanov 1994). Since the turbulent state is characterised by a higher friction coefficient, delaying the transition to turbulence would result in a reduction of the friction drag and, thus, in a potential energy saving. In addition to passive methods, in recent decades researchers have explored active control strategies for TSW attenuation, spanning from optimal control (e.g. Sharma *et al.* 2011; Semeraro *et al.* 2013) to wave cancellation (e.g. Sturzebecher & Nitsche 2003; Kotsonis, Shukla & Pröbsting 2015; Simon *et al.* 2016). Although effective and relatively robust in delaying transition, these approaches often suffer from poor overall energy efficiency due to limitations in actuator technology (Fabbiane, Bagheri & Henningson 2017). Also because of these limitations, researchers have recently revived interest in passive techniques – such as compliant walls – that do not require external energy to operate.

When considering the interaction between a boundary-layer flow and a compliant wall, the flexibility of the latter plays a pivotal role in the attenuation of TSWs, where increased compliance leads to a larger stabilisation of the fluid instability (Carpenter & Garrad 1985; Yeo 1988). However, the compliance of the wall introduces additional instabilities due to fluid–structure interaction between the boundary layer and the compliant wall (Benjamin 1963; Carpenter & Garrad 1986). Historically, these instabilities have been categorised following the three-fold classification introduced by Benjamin (1960) and later illustrated from an energy transfer standpoint by Benjamin (1963). The stability characteristics of the first two groups depend on the non-conservative energy transfer between and within the fluid flow and the compliant solid; the third group, instead, relates to conservative energy exchanges between the two phases. The first type collects instabilities already present in the flow and modified by the interaction with the compliant wall, such as TSWs, as well as static divergence. The development of these instabilities requires a negative variation of the total energy of the fluid–structural system and, as such, dissipation in the compliant wall will result in their destabilisation (Yeo & Dowling 1987). The second type groups instabilities, comprising travelling-wave flutter (TWF), linked to a positive variation of the total energy of the fluid–structural system and, by consequence, stabilised by the dissipative behaviour of the solid phase. The third, and last, type of instabilities (akin to the inviscid Kelvin–Helmholtz instability; Gad-el Hak 1996) is a consequence of unidirectional conservative energy exchanges to the solid and can be avoided by reducing the flexibility of the wall. Among these, TWF can be very insidious in transition-delay applications, as it can lead to a premature laminar-to-turbulent transition in real experimental scenarios (Lucey & Carpenter 1995). Structural viscosity, achievable through the use of viscoelastic materials, has been shown to mitigate TWF but at the expense of a compromised TSW attenuation (Carpenter & Garrad 1986). A comprehensive review of the progress in the field up to the end of the twentieth century is provided by Carpenter, Lucey & Davies (2001). More recent investigations (Tsigklifis & Lucey 2017; Pfister, Fabbiane & Marquet 2022) have confirmed the role of structural compliance and viscosity in both TSWs and TWF, adopting a novel approach that emphasises forced responses over traditional modal stability analysis. Notably, these new numerical tools, as developed by Pfister, Marquet & Carini (2019) and applied by Pfister *et al.* (2022), now facilitate the global stability analysis of the coupled fluid–structural problem. These advancements offer two significant advantages: they allow one to take into account the non-parallel nature of the boundary-layer flow, providing a more realistic representation; and they open the way for exploring more complex configurations of the solid phase, such as compliant surfaces made by microstructured compliant layers.

The study of microstructured (visco)elastic media has been the focus of very intense research in past decades for various applications spanning from electromagnetism to acoustics, under the name metamaterials. These metamaterials are periodic arrangements of materials that allow the control of the behaviour of waves (acoustic, elastic or electromagnetic) in a desirable and usually surprising way, in a sense impossible to obtain with a homogeneous material. Particularly striking realisations of metamaterials are invisibility cloaks (Schurig *et al.* 2006; Ni *et al.* 2015) or negative refractive index materials (Smith, Pendry & Wiltshire 2004; Dolling *et al.* 2006; Brunet, Leng & Mondain-Monval 2013), allowing one to bend light or sound waves (Smith *et al.* 2004; Pendry, Luo & Zhao 2015; Colombi *et al.* 2016) and render details finer than the used wavelength of light (Pendry & Smith 2006). In terms of modelling, metamaterials are studied using Floquet–Bloch analysis, by which the entire structure can be understood on the basis of calculus performed on the periodicity cell (Collet *et al.* 2011). One of the features often observed and desired in metamaterials is the appearance of band gaps, that is to say, frequency intervals at which waves cannot propagate, and rather localise in the form of evanescent waves. This is the phenomenological feature that motivates the use of a metamaterial as a compliant surface at the boundary of a flow.

Metamaterials have already found their way to flow control, with a growing number of examples of their potential applications in the literature. Recent studies have proposed the use of metamaterials in a diverse range of flow control scenarios, including the mitigation of flow-induced vibrations (Piest, Druetta & Krushynska 2024) and the reduction of shock-induced vibrations (Navarro *et al.* 2025). In the last few years, the attenuation of TSWs has also garnered attention within the metamaterials community. In particular, the research on this topic has focused on the use of a specific type of metamaterial structure, phononic subsurfaces, as firstly proposed by Hussein *et al.* (2015) in a channel flow. In that study, a periodic stacking of layers of different materials is used to create a phononic crystal (Hussein, Leamy & Ruzzene 2014). One end of the resulting one-dimensional crystal is then made to locally interact with the flow perturbation at the wall, in order to attenuate the incoming TSWs by means of an anti-resonant interaction with the structure. This leads to a configuration in which the phonon develops below the surface along the wall-normal direction, leading to the designation phononic subsurface (Hussein *et al.* 2015). A key advantage of this set-up is the avoidance of TWF issues, achieved through the localised interaction between the phononic subsurface and the fluid. Nevertheless, a significant challenge lies in the size of the employed phononic crystal, which may not be suitable for aeronautical applications; however, recent research has made progress in overcoming this limitation using compact local-resonating phononic metamaterials that maintain performance (Kianfar & Hussein 2023). Unfortunately, a further potential drawback of this layout is the possible (re-)amplification of the TSW downstream the interaction point, which could invalidate the intended control effect (Michelis, Putranto & Kotsonis 2023).

The current study aims to integrate the recent introduction of phononic subsurfaces in flow control with the more consolidated research on compliant walls for TSW attenuation. We therefore propose a different strategy, where the wall compliance is used to attenuate TSWs and the wave-blocking properties of phononic metamaterials to mitigate the undesired TWF. As a starting point, we consider the conventional configuration proposed by Pfister *et al.* (2022), with a finite-length, homogeneous, compliant patch installed at the wall interacting with a zero-pressure-gradient boundary-layer flow (figure 1). However, our approach employs a phononic structure, created by incorporating stiff elements into a homogeneous viscoelastic matrix (figure 1*b*), differing from the conventional compliant surface in figure 1(*a*). Therefore, the wave-blocking capabilities along the periodic
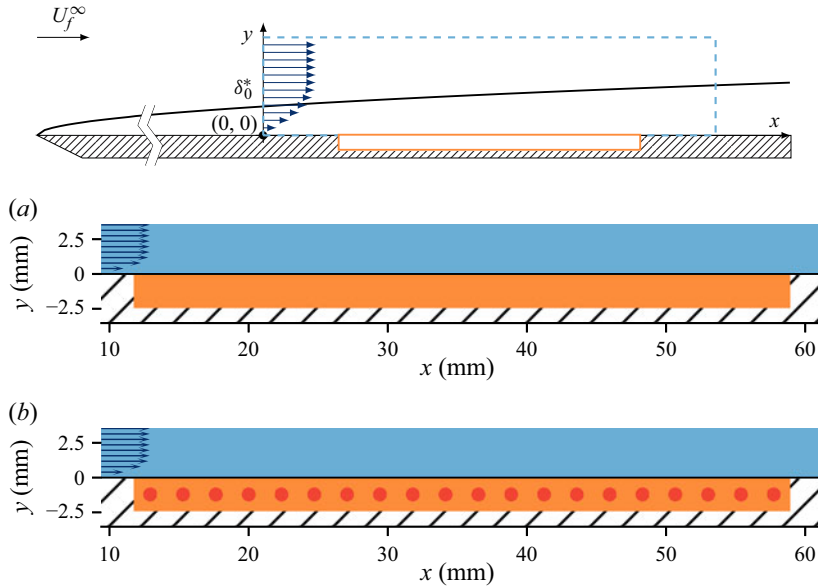
Figure 1. Wall-mounted compliant wall (orange) in a zero-pressure-gradient boundary-layer flow in water (blue). The origin of the frame of reference is positioned at the wall at the beginning of the computational domain: x and y indicate, respectively, the streamwise and wall-normal coordinates. The leading edge of the plate (i.e. the origin of the boundary layer) is positioned at $x \approx -47.7$ cm, for a uniform free-stream velocity $U_f^\infty = 10$ m s^{-1}. The resulting Reynolds number based on the displacement thickness at the inflow (δ_0^*) is $Re_{\delta_0^*} = 3000$. (*a*) The conventional set-up from Pfister *et al.* (2022) with a compliant structure made by a homogeneous viscoelastic material. (*b*) The phononic compliant surface obtained by introducing stiffer inclusions (in red) within the homogeneous matrix and the subject of the current study.

direction are used to prevent wave propagation in the solid phase that contributes to TWF onset. This approach exploits a more direct utilisation of the phononic surface's unique dynamics and introduces a distinct fluid–solid interaction paradigm, where the phonon couples with the fluid along the wave-propagation direction within the solid. Notably, this difference is underscored by our layout, where the phononic surface aligns with the wall, contrasting with the wall-normal orientation that can be found in the current literature (Hussein *et al.* 2015; Kianfar & Hussein 2023; Michelis *et al.* 2023).

The rest of the article is structured as follows. Section 2 introduces the phononic compliant surface and compares it with the conventional one from Pfister *et al.* (2022), through global stability and resolvent analyses. Section 3 discusses the design principles underlying the phononic surface, utilising Bloch analysis as a primary design methodology, which is validated through comparison with global stability analysis. Concluding remarks and perspectives are presented in §4. Additional technical details regarding the governing equations and numerical methods employed in the fluid–structural analysis can be found in Appendix A.

2. A phononic compliant surface to attenuate boundary-layer flow instabilities

We consider the configuration illustrated in figure 1 for the numerical investigation of the passive control of the laminar-to-turbulent transition with compliant surfaces in a zero-pressure boundary-layer flow. A water flow of density $\rho_f = 1000$ kg m^{-3}, viscosity $\mu_f = 1.569$ mPa s and uniform velocity $U_f^\infty = 10$ m s^{-1} encounters the leading edge of

a flat plate where a boundary layer starts to develop. According to Blasius boundary-layer theory (Schlichting & Gersten 2016), its displacement thickness increases as $\delta^*(d) = 1.72 \, (v_f \, d/U_f^\infty)^{1/2}$, where $v_f = \mu_f/\rho_f$ is the kinematic viscosity of the fluid and d is the distance from the leading edge. The displacement thickness is equal to $\delta_0^* = 0.471$ mm at a distance of $1014 \, \delta_0^* = 47.7$ cm, where the centre of our coordinate system (x, y) is located, as reported in figure 1. This location corresponds to the inlet boundary of the computational domain for the flow, which is then characterised by the non-dimensional Reynolds number $Re_{\delta_0^*} = U_f^\infty \, \delta_0^*/v_f = 3000$. For that Reynolds number, TSWs are expected to grow in the zero-pressure-gradient boundary layer for frequencies within the range 80 Hz $\leq f \leq$ 300 Hz and wavelengths 9 mm $\leq \lambda_x \leq$ 30 mm (Schmid & Henningson 2001). To capture those flow instabilities, the computational domain in the fluid side (delimited with dashed blue lines in the figure) extends up to $y = 14.1$ mm in the wall-normal direction and $x = 84.7$ mm in the streamwise direction.

2.1. *Conventional and phononic compliant surfaces*

To attenuate the amplification of these TSWs in the boundary-layer flow, a compliant structure of fixed length ($l = 47.1$ mm) and depth ($h = 2.35$ mm) is flush-mounted at the wall starting at a distance $x = 11.8$ mm from the inlet of the computation domain, i.e. the origin of our coordinate system. Length, depth and location of the compliant walls are chosen to match to those employed by Pfister *et al.* (2022) and they correspond to $100\delta_0^*$, $5\delta_0^*$ and $25\delta_0^*$, respectively. Two different structures – schematically illustrated in figure 1 – are then considered to delay the laminar-to-turbulent transition: a conventional compliant surface (figure 1*a*) obtained by considering a structure made of a homogeneous soft material and a phononic compliant surface (figure 1*b*) obtained by periodically placed, stiffer inclusions in the soft material.

The conventional compliant surface, illustrated in figure 1(*a*), is obtained here by using a soft elastomer (Ashby 1999). More specifically, the density of this soft elastomer is chosen as $\rho_s = 1000$ kg m^{-3}, i.e. equal to the density of water ρ_f. Its elastic and viscous properties are defined through the Young's modulus $E_s = 0.1$ MPa and the material viscosity $D_s = 0.94$ Pa s, respectively. Additionally, elastomers are usually modelled as incompressible materials and, thus, a Poisson coefficient $v_s = 0.5$ is considered. This specific choice corresponds to that proposed by Pfister *et al.* (2022). In particular, their work showed numerically that the flexibility of the compliant surface allows one to attenuate the amplification of TSWs occurring at low frequency of around $f \sim 200$ Hz, with a streamwise wavelength $\lambda_{TSW} \approx 30\delta_0^* = 14.1$ mm; this resulted in a ratio between the length of the compliant wall (l) and the TSW wavelength (λ_{TSW}) of about 3. Meanwhile, the viscosity of the compliant surface prevents the destabilisation of natural vibration modes of the structure by the flow at higher frequencies $f \sim 1300$ Hz. Still, the structural viscosity is not large enough to avoid the amplification of the so-called TWF instabilities by an external forcing in the flow. These TWF instabilities propagate in the streamwise direction in the vicinity of the fluid–solid interface and are characterised by a streamwise wavelength $\lambda_x \sim 4.7$ mm, for the current choice of dimensional parameters.

The phononic compliant surface, illustrated in figure 1(*b*), is here introduced to specifically attenuate the amplification of TWF instabilities. The term phononic refers to metamaterials or structures that possess an inherent periodicity in their internal geometry (Hussein *et al.* 2014). This periodicity, when properly tuned, imparts unique dynamical properties, such as blocking the propagation of waves in specific directions and frequency ranges. In the case of TWF instabilities, we exploit the wave-blocking properties of phononic materials to prevent the streamwise propagation of solid waves

N. Fabbiane, O. Marquet, L. Pierpaoli, R. Cottereau and M. Couliou

in the phononic compliant surface. Thus, we aim at breaking the unstable interaction between natural vibration modes of the surface and flow perturbations. To that aim, we add circular inclusions (red circles) made of a stiffer material ($E_I = 1$ MPa) into a homogeneous matrix (orange) made from the same material ($E_s = 0.1$ MPa) as that used for the conventional homogeneous compliant surface. The two materials (matrix and inclusions) share the same density ($\rho_I = 1000$ kg m^{-3}); note that the stiffer material corresponds to common elastomers such as natural rubber or polydimethylsiloxane. These circular inclusions have a diameter $d_I = 0.94$ mm and they are periodically placed in the streamwise direction with a constant spacing of $l_I = 2.35$ mm, so as to achieve the band-gap properties of the phononic surface for TWF of wavelength $\lambda_x = 4.7$ mm. The details of the design process that led to the considered spacing of the circular inclusions are addressed in § 3. The phononic compliant surface is finally made of 20 inclusions that are periodically arranged in the same direction as the flow. This is different from the phononic surface first proposed by Hussein *et al.* (2015) and later by Michelis *et al.* (2023) who introduced a periodic arrangement of material in the wall-normal direction to attenuate TSWs. With our phononic compliant surface, the natural compliance of the matrix materials should still be exploited to attenuate those waves, as in the case of the conventional compliant surface.

2.2. *Linear fluid–structure perturbations: global stability and resolvent analyses*

The interaction of these compliant surfaces with flow perturbations developing in the boundary layer are investigated numerically based on the framework detailed in Appendix A. It was first developed by Pfister *et al.* (2019) for the study of vortex-induced vibrations of a thin plate and later applied to the control of boundary-layer flow instabilities with a conventional homogeneous compliant surface (Pfister *et al.* 2022). Similar theoretical and numerical tools have also been used in the literature for the study of the dynamics of gas bubbles in straining flows (Sierra-Ausin *et al.* 2022). The equations governing the interaction between an incompressible flow and a hyperelastic structure are written in the arbitrary Lagrangian–Eulerian (ALE) framework. To investigate the linear dynamics of flow perturbations interacting with solid perturbations, these equations are linearised around steady solutions of the coupled fluid–structural equations. In the present case, the static deformation $\boldsymbol{\Xi}_s(\boldsymbol{x})$ of both compliant surfaces induced by the zero-pressure-gradient boundary-layer flow remains small with respect to the boundary-layer thickness ($|\boldsymbol{\Xi}_s| < 10^{-3} \, \delta_0^*$), thus confirming the assumption made in Pfister *et al.* (2022) of an non-deformed compliant wall. The linear dynamics of coupled fluid–structure perturbations is then investigated based on (i) global stability analysis to determine the onset of self-sustained fluid–structure oscillations and (ii) resolvent analysis to investigate the amplification of flow perturbations sustained by an external forcing, in the case of globally stable steady solution.

The equations governing infinitesimal flow perturbations $\boldsymbol{q}'_f$ and solid perturbations $\boldsymbol{q}'_s$ of the steady flow state $\boldsymbol{Q}_f$ may be written as the coupled linear equations

$$
\begin{bmatrix} \boldsymbol{B}_f & 0 \\ 0 & \boldsymbol{B}_s \end{bmatrix} \frac{\partial}{\partial t} \begin{bmatrix} \boldsymbol{q}'_f \\ \boldsymbol{q}'_s \end{bmatrix} - \begin{bmatrix} \boldsymbol{A}_f(\boldsymbol{Q}_f) & \boldsymbol{C}_{fs} \\ \boldsymbol{C}_{sf} & \boldsymbol{A}_s \end{bmatrix} \begin{bmatrix} \boldsymbol{q}'_f \\ \boldsymbol{q}'_s \end{bmatrix} = \begin{bmatrix} \boldsymbol{P}_f \\ 0 \end{bmatrix} \boldsymbol{f}', \quad (2.1)
$$

where the first line corresponds to the linearised ALE incompressible Navier–Stokes equations while the second line corresponds to the linear viscoelastic equations (Kelvin–Voigt model). The exact definitions of the operators are detailed in Appendix A. The right-hand side forcing term $\boldsymbol{f}'$ corresponds to an external forcing in the momentum flow

equations that is introduced for the resolvent analysis but is dropped in the global stability analysis.

In the global stability analysis, the long-term temporal amplification or decay of linear fluid–structural perturbations is investigated by assuming an exponential temporal growth of perturbations as

$$
\begin{bmatrix} q'_f(x,t) \\ q'_s(x,t) \end{bmatrix} = \begin{bmatrix} \tilde{q}_f(x) \\ \tilde{q}_s(x) \end{bmatrix} \mathrm{e}^{(\gamma+\mathrm{i}\omega)\,t} + \underbrace{\begin{bmatrix} \tilde{q}_f^*(x) \\ \tilde{q}_s^*(x) \end{bmatrix} \mathrm{e}^{(\gamma-\mathrm{i}\omega)\,t}}_{\text{complex conjugate (c.c.)}}, \tag{2.2}
$$

where ω (γ) is the frequency (growth rate) associated with the complex spatial structures denoted $\tilde{q}_f$ in the flow and $\tilde{q}_s$ in the solid. In the following, terms like the under-braced expression will be abbreviated as 'c.c.', indicating that they represent the complex conjugate of their preceding term. Injecting the above decomposition into (2.1) yields the following coupled fluid–structural eigenvalue problem:

$$
(\gamma + \mathrm{i}\omega) \begin{bmatrix} B_f & 0 \\ 0 & B_s \end{bmatrix} \begin{bmatrix} \tilde{q}_f \\ \tilde{q}_s \end{bmatrix} - \begin{bmatrix} A_f(Q_f) & C_{fs} \\ C_{sf} & A_s \end{bmatrix} \begin{bmatrix} \tilde{q}_f \\ \tilde{q}_s \end{bmatrix} = \begin{bmatrix} 0 \\ 0 \end{bmatrix}. \tag{2.3}
$$

In the resolvent analysis, we investigate the linear response of the fluid and solid perturbations to external forcing, that is here restricted to the momentum flow equations. The forcing and response may be decomposed into temporal harmonics as

$$
f'(x,t) = \hat{f}(x)\,\mathrm{e}^{\mathrm{i}\omega t} + \text{c.c.} \quad \text{and} \quad \begin{bmatrix} q'_f(x,t) \\ q'_s(x,t) \end{bmatrix} = \begin{bmatrix} \hat{q}_f(x) \\ \hat{q}_s(x) \end{bmatrix} \mathrm{e}^{\mathrm{i}\omega t} + \text{c.c.}, \tag{2.4}
$$

where the forcing frequency, also denoted ω, is now a parameter, while $\hat{f}$, $\hat{q}_f$ and $\hat{q}_s$ are spatial structures. The latter are related by the following input–output relation that is obtained after injecting the above harmonic decomposition into (2.1):

$$
\begin{bmatrix} \hat{q}_f \\ \hat{q}_s \end{bmatrix} = R_{fs}(\omega)\,P\hat{f}, \quad \text{where} \quad R_{fs}(\omega) = \left(\mathrm{i}\omega \begin{bmatrix} B_f & 0 \\ 0 & B_s \end{bmatrix} - \begin{bmatrix} A_f(Q_f) & C_{fs} \\ C_{sf} & A_s \end{bmatrix} \right)^{-1} \tag{2.5}
$$

is the aeroelastic resolvent operator and $P = [P_f, 0]^T$ is a prolongation operator allowing one to impose the forcing solely on the fluid momentum equations. The resolvent analysis (Sipp & Marquet 2013) consists here of identifying, for each forcing frequency $\omega = 2\pi f$, the spatial structure $\hat{f}$ of the forcing that provides the largest energy amplification σ^2 of the flow velocity perturbation $\hat{u}_f$, a component of $\hat{q}_f$. The energy gain is defined as

$$
\sigma^2(\omega) = \max_{\hat{f}} \left(\frac{\|\hat{u}_f\|^2}{\|\hat{f}\|^2} \right) \quad \text{with} \quad \|\hat{u}_f\|^2 = \int_{\Omega_f} \hat{u}_f^* \cdot \hat{u}_f \, \mathrm{d}\Omega = \hat{q}_f^* \, M_u \, \hat{q}_f,
$$

$$
\|\hat{f}\|^2 = \int_{\hat{\Omega}_f} \hat{f}^* \cdot \hat{f} \, \mathrm{d}\Omega = \hat{f}^* \, M_f \, \hat{f}. \tag{2.6}
$$

Here $\|\hat{f}\|^2$ is the norm of the forcing field and $\|\hat{u}_f\|^2$ is the norm of the harmonic fluid velocity perturbation $\hat{u}_f$. In order to limit the influence of the outflow boundary condition on the amplification factor σ, the fluid domain $\hat{\Omega}_f$ utilised for computing the two norms is truncated at $x = 70.6$ mm. As shown by Brandt *et al.* (2011), the optimal flow forcing and response can be determined by computing the largest eigenvalue σ^2 of the Hermitian eigenvalue problem

N. Fabbiane, O. Marquet, L. Pierpaoli, R. Cottereau and M. Couliou

$$P^T R_{fs}^H(\omega) M_u R_{fs}(\omega) P\hat{f} = \sigma^2 M_f \hat{f}. \tag{2.7}$$

In the following, we solve numerically the here-presented problems using a first-order (pressure) and second-order (fluid velocity and solid displacement) continuous-Galerkin finite-element method through the DOLFINx library (Baratta *et al.* 2023). The resulting eigenvalue problems are solved with SLEPc's Krylov–Schur algorithm (Roman *et al.* 2023).

2.3. *Results*

Let us first examine the effect of the conventional compliant surface, made with a homogeneous viscoelastic material as illustrated in figure 1(*a*), on the amplification of perturbations in the boundary-layer flow. Figure 2(*a*) displays the optimal amplifications σ, as a function of the frequency $f = \omega/2\pi$, of forced harmonic flow perturbations developing in the boundary layer over the rigid surface (blue dotted curve) and the conventional homogeneous compliant surface (black dashed curve). The amplification of TSWs corresponds to the peak observed at low frequency $f \approx 210$ Hz. Maximal for the rigid surface, the magnitude of this peak is clearly reduced when using the conventional compliant surface. This result, introduced in Pfister *et al.* (2022), shows the potential of compliant surfaces for delaying the laminar-to-turbulent transition of boundary layers induced by TSWs.

However, for the conventional compliant wall, that effect may be undermined by the appearance of a second peak around the higher frequency $f = 1350$ Hz. This amplification of flow perturbation at higher frequency is associated with a flow-induced surface instability first identified by Benjamin (1960). Later termed the TWF instability (Carpenter & Garrad 1985; Tsigklifis & Lucey 2017), it involves perturbations in both fluid and solid phases that manifest as travelling waves localised near the fluid–solid interface. As shown in figure 2(*c*), these waves, characterised by a (dimensional) wavelength $l_{TWF} \approx 4.5$ mm, propagate along the boundary layer while undergoing amplification. The observed energy amplification of the flow response to external flow forcing at high frequencies can be interpreted as a modal resonance. The eigenvalues of the coupled fluid–structural problem, that describe the self-sustained dynamics (i.e. without external forcing) of the boundary-layer flow perturbations interacting with the conventional compliant surface, are shown in figure 2(*b*) (black crosses). The eigenvalue branch near the frequency $f = 1350$ Hz corresponds to structural vibration modes coupled with the fluid. As shown by Pfister *et al.* (2022), this branch becomes unstable (with positive growth rates) when the compliant surface is made of a purely elastic material. In contrast, when a viscoelastic material is used, as in the present configuration, the same branch remains stable (with negative growth rates). This means that, without an external forcing, small perturbations of the coupled system will eventually decay in time because of the effect of the material viscosity. Although structural damping due to material viscosity stabilises these eigenmodes, a resonance still arises in the forced response of the flow. This is reflected in the pronounced peak centred around $f = 1350$ Hz in the dashed curve of figure 2(*a*). Designing compliant surfaces with more viscous materials may further stabilise this eigenvalue branch and thereby reduce the amplification of externally forced flow perturbations. However, an increase of the structural damping would lead to a destabilisation of the TSW (Yeo & Dowling 1987). Therefore, we propose to leverage the dynamical properties of phononic surfaces to mitigate the amplification of the TWF instability at high frequency, while preserving the favourable influence of compliant surfaces on low-frequency TSW instability.
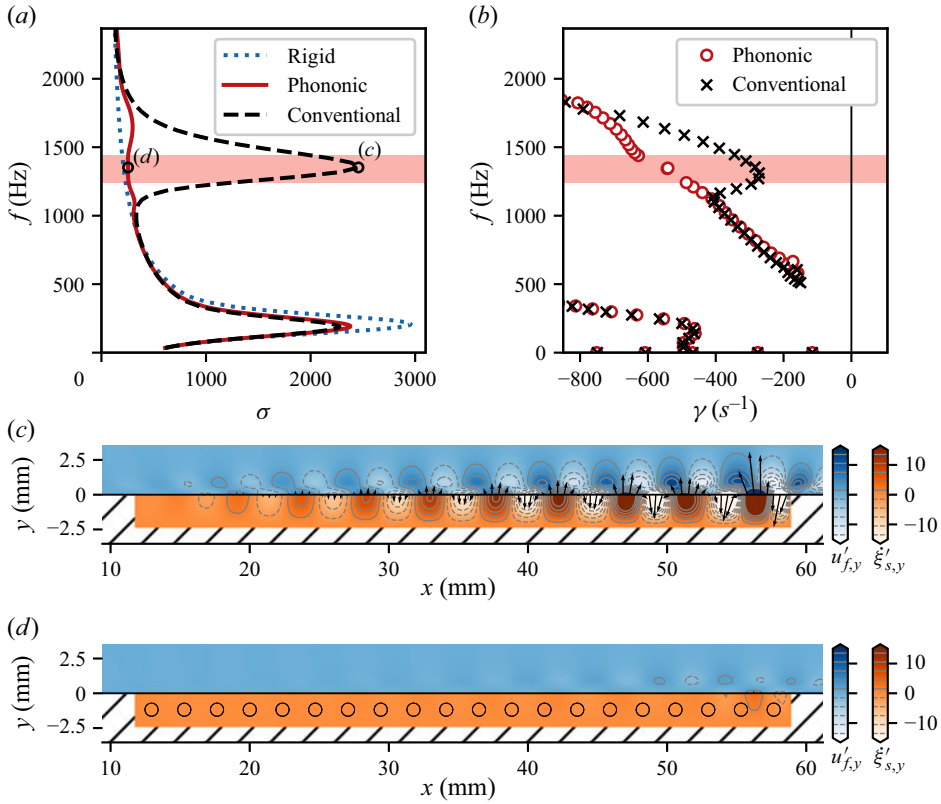
Figure 2. Global, coupled, linear stability analyses of the conventional and phononic compliant surfaces in figure 1 interacting with a laminar boundary-layer flow. The optimal, harmonic, forced response (*a*) and eigenvalue analysis (*b*) are reported for the conventional compliant surface (black dashed line and crosses) and the phononic one (red solid line and white-filled, red circles). The blue dotted line in (*a*) indicates the response over a rigid wall. The spatial structure of the response of the fluid–structural system at the TWF amplification peak ($f \approx 1350$ Hz) is reported for both the conventional (*c*) and phononic (*d*) compliant surfaces. The colour indicates the real part of the vertical velocity in the fluid (blue) and solid (orange) phases, while the black vectors the real part of the surface displacement at the interface. The red shaded area in (*a,b*) indicates the identified band gap of the phononic surface (1241 Hz $\leq f \leq$ 1439 Hz), encompassing the two truncation modes (see figure 3).

The open red circles in figure 2(*b*) display the fluid–solid eigenvalue spectrum obtained with the phononic compliant surface. The bump in the growth rate previously observed along the branch of fluid–solid modes for the conventional compliant surface (black crosses in figure 2*b*) is no longer present. Instead, a gap appears in the eigenvalue branch between 1241 and 1439 Hz, as highlighted by the red shaded region (see § 3 for definition and further details). Within this frequency range, only two isolated eigenmodes are found at $f = 1343$ Hz and $f = 1347$ Hz, both having near-identical eigenvalues. Their spatial structures, shown in figure 3, reveal high amplitudes localised at the upstream and downstream edges of the compliant surface. The modes result from truncation resonance (Rosa *et al.* 2023), a phenomenon inherent to finite-sized phononic materials, which is further discussed in a later section (see § 3.3). The band gap in the eigenvalue spectrum is centred (by design, see § 3) precisely around the frequency at which TWF instabilities are strongly amplified in the case of the conventional compliant surface. This effect arises from a key property of phononic materials: their ability to inhibit the propagation of waves
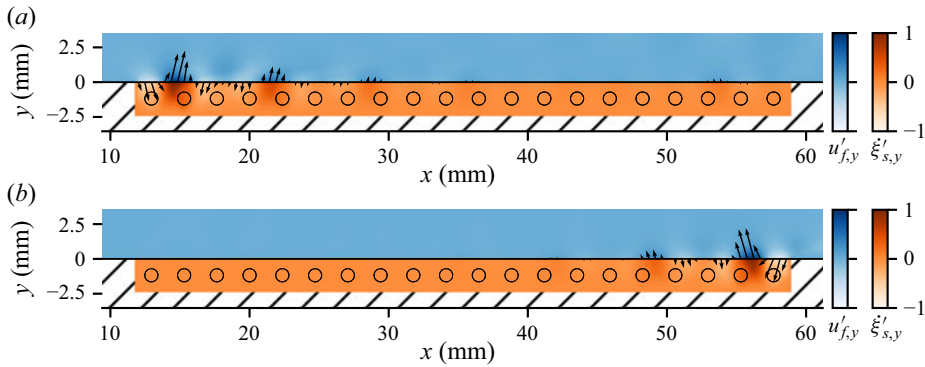
Figure 3. Truncation eigenmodes from the coupled fluid–structural interaction of the phononic compliant surface with the boundary-layer flow (see figure 2b). The colour reports the real part of the vertical velocity in the fluid (blue) and solid (orange) phases; the black vectors indicate the real part of the surface displacement at the interface. The reported modes occur at $f = 1343$ Hz (a) and $f = 1347$ Hz (b).

with specific wavelengths, thereby suppressing the emergence of natural vibration modes at targeted frequencies.

We now examine the impact of this band gap on the amplification of flow perturbations over the phononic compliant surface when excited by an external harmonic forcing. The red solid curve in figure 2(a) presents the optimal amplification σ in the presence of the phononic compliant surface. The prominent peak observed near $f = 1350$ Hz in figure 2(a) has entirely vanished, while the attenuation of Tollmien–Schlichting instabilities is preserved at lower frequency ($f \approx 210$ Hz). Figure 2(d) shows the spatial structure of the fluid and solid perturbations in response to optimal external flow forcing at that frequency. A spatially growing surface wave characterised by a distinct wavelength of approximately $l_{TWF} \approx 4.5$ mm is still observed but with a magnitude strongly reduced compared with the case of the conventional compliant surface (figure 2c). One should note that the observed wavelength is approximately twice the spacing l_I between the periodic inserts that constitute the phononic surface (grey lines in figure 2d). This correspondence can be attributed to the relationship in phononic media between the frequency intervals of band-gap appearances and the wavelength of the blocked solid wave, which in turn is linked to its intrinsic periodicity (Hussein *et al.* 2014). These results demonstrate that the proposed phononic compliant surface, specifically designed to introduce a band gap in the eigenvalue spectrum at the frequency of TWF instability, effectively suppresses its amplification. Crucially, this is achieved without compromising the compliant nature of the surface, and therefore retain its beneficial influence on the control of low-frequency TSWs.

It is then of interest to evaluate the performance of the phononic compliant surface not only on the attenuation of TWF, but also of TSWs. Figure 4(a) reports the response of the coupled system over the phononic surface for the optimal response at the TSW amplification peak ($f = 210$ Hz, as identified in figure 2a); the blue colours indicate the streamwise component of the velocity perturbation in the fluid, while the orange the vertical component in the solid. It is observed that the TSW interacts with the compliant wall over more than three wavelengths and the solid responds to the perturbation in a similar manner. According to the analyses by Pfister *et al.* (2019), the response of the compliant wall induces a counter-phase TSW, which results in an attenuation of the perturbation in the fluid. This is reflected in the attenuation of the amplification factor σ (reported in figure 2a), which indicates that the integrated magnitude of the velocity perturbation field in the fluid domain is reduced and, therefore, a global attenuation of
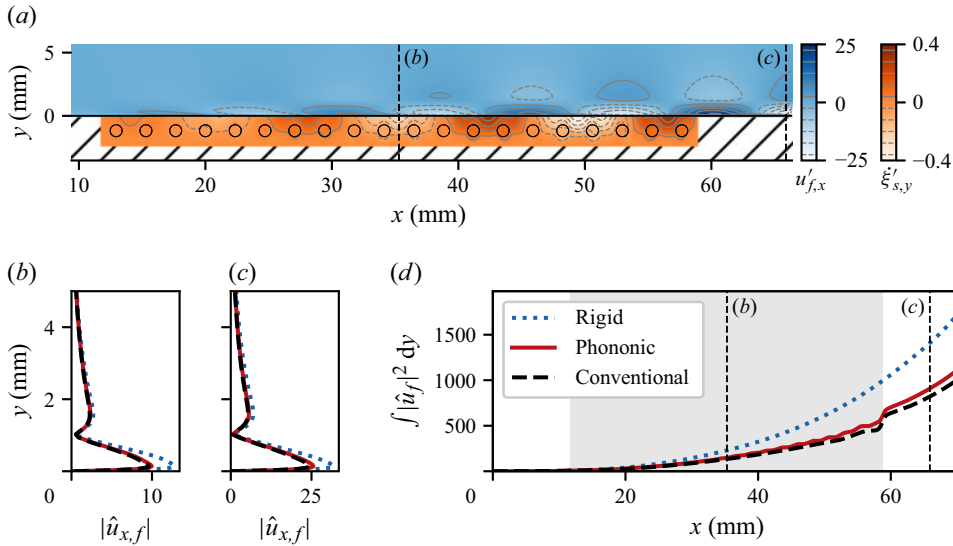
Figure 4. Spatial attenuation of TSWs. (*a*) The perturbation fields over the phononic surface for the optimal, harmonic, forced response at the amplification peak of TSWs, $f = 210$ Hz in figure 2. The colour shows the streamwise component of the perturbation velocity in the fluid ($u'_{f,x}$, in blue) and the vertical component of the solid velocity ($\dot{\xi}'_{s,y}$, in orange). The magnitude of the streamwise velocity perturbation field at (*b*) $x = 35$ mm and (*c*) $x = 66$ mm. The dotted, dashed and solid curves indicate, respectively, the rigid, conventional compliant and phononic compliant surfaces. (*d*) The integrated amplitude of the velocity perturbation in the fluid phase; the grey area indicates the streamwise extent of both the conventional and the phononic compliant walls.

TSWs is observed. Nevertheless, this quantity does not provide any information on spatial amplification. To better characterise this aspect, the streamwise component of the velocity perturbation in the fluid is extracted, for the responses at $f = 210$ Hz, at two different streamwise locations: in the middle of the compliant walls at $x = 35$ mm (figure 4*b*) and downstream of them at $x = 66$ mm (figure 4*c*). In accordance with Pfister *et al.* (2022), at both locations the TSW presents with a reduced amplitude with respect to the rigid-wall case (blue dotted line) when a compliant wall is considered (black dashed line, conventional; dashed red line, phononic). Notably, the TSW over the compliant walls presents with its typical modal shape, as over the rigid wall. To complete the analysis, figure 4(*d*) illustrates the streamwise development of the velocity perturbation energy, integrated along the wall-normal direction. For context, the blue dotted line represents the spatial growth of TSW over a rigid wall, which, in accordance with conventional stability theory, exhibits exponential-like behaviour along the streamwise direction (Schmid & Henningson 2001). In contrast, the dashed and solid lines denote the responses for the conventional compliant wall and the phononic surface, respectively. Notably, both compliant surfaces demonstrate comparable attenuation of TSW growth within the compliant wall's extent (grey region), relative to the rigid-wall scenario. This reduced amplitude persists downstream of the patch location, indicating that TSWs interacting with either the conventional or the phononic compliant surface will exhibit delayed breakdown to turbulence, compared with those interacting with a rigid wall. We note that a localised increase in amplitude is present at the trailing edge of the compliant surfaces, specifically at $x \approx 59$ mm. This phenomenon bears resemblance to observations in studies focused on controlling TSWs through localised flow interaction with a phononic subsurface (Michelis *et al.* 2023). In those contexts, such localised amplification limits the

effective implementation of the proposed flow control principle. Recent developments, exploring combined streamwise and spanwise patterns of localised phononic subsurfaces, suggest potential strategies for mitigating this issue (Hussein *et al.* 2025). Nonetheless, in the current configuration featuring a streamwise-extended phononic surface, despite a slight reduction in overall performance, this aspect does not pose a significant limitation to utilising compliant walls for TSW attenuation. While TSW attenuation is common to the two investigated compliant surfaces, conventional and phononic, the phononic one avoids the TWF amplification characteristic of its conventional counterpart. Given that TWF can trigger premature laminar-to-turbulent transition (Lucey & Carpenter 1995), a genuine transition delay is only achievable with the employment of the phononic compliant surface.

In the following section, we recall and discuss in further detail the principles that led to the design of the phononic surface, namely the relation between the periodic structure of the phononic surface and its dynamical properties by means of Bloch analysis.

3. Design of the phononic surface based on Bloch analysis

Having demonstrated that our finite-sized phononic compliant surface effectively suppresses the amplification of TWF instabilities – while preserving the attenuation of low-frequency TSWs – we now provide a more detailed description of its design principles. As previously discussed, this design leverages the wave-blocking properties of phononic metamaterials to inhibit the propagation of solid waves. More specifically, by preventing wave propagation in the streamwise direction at the frequencies where TWF instabilities typically develop and amplify, the goal is to disrupt the modal resonance mechanism responsible for their strong amplification, and thus to effectively suppress these instabilities. Our phononic compliant surface builds upon the conventional homogeneous compliant surface introduced by Pfister *et al.* (2022), which consists of a homogeneous viscoelastic material. The elastic and viscous properties of this material were specifically chosen to attenuate both low-frequency TSWs and high-frequency TWF instabilities. To introduce streamwise periodicity into this viscoelastic matrix, we embed circular scatterers made of a stiffer material, as previously illustrated in figure 1(*b*). While this particular geometric arrangement is somewhat arbitrary, its key advantage lies in preserving the overall compliance of the fluid–solid interface, thereby maintaining the beneficial damping effect on TSWs. Once the geometry of the inclusions is fixed, the design problem reduces to specifying the spacing l_I between inclusions and their stiffness, characterised by the Young's modulus E_I of the inclusion material. It is therefore crucial to establish a relationship between these design parameters and the wave-blocking properties of the resulting phononic metamaterial. To this end, we employ Bloch analysis, which relies on the assumption of an infinitely extended structure along the periodicity direction. This simplification reduces the wave propagation problem to the study of a single unit cell, thereby significantly lowering the computational cost and making the method particularly suitable for design and optimisation.

In the following, our objective is to gain physical insight into the mechanisms underlying the wave-blocking behaviour of the phononic surface. We start by introducing the theoretical formalism for the Bloch analysis of the phononic surface (§ 3.1). Subsequently, the results from the analysis are presented in § 3.2, with a particular focus on the sensitivity of the band gap to variations in the design parameters, which informs the identification of the proposed configuration (§ 3.2.3). Finally, we compare the wave dynamics between infinite and finite phononic surfaces to evaluate the robustness of the design in practical implementations (§ 3.3).
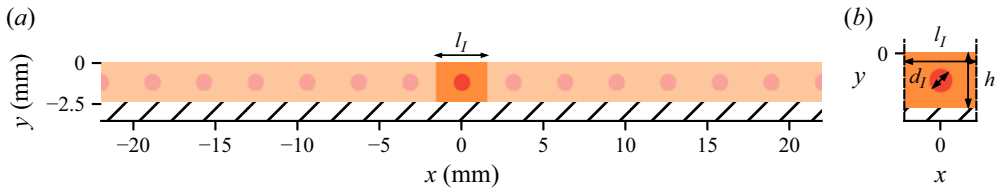
Figure 5. Infinite, periodic, phononic surface. The periodic cell (*b*) – clamped at the bottom and free at the top – with span l_I is periodically and infinitely replicated along the x direction (*a*).

3.1. *Bloch analyses of the phononic compliant surface*

We here consider two different scenarios for the Bloch analysis of the phononic compliant surface. The first involves only the periodic elastic medium, isolated from the fluid domain and subject to a stress-free boundary condition (§ 3.1.1). The second incorporates the interaction with the fluid, but it considers as a base state a fluid with no flow, i.e. at rest (§ 3.1.2). The Bloch analysis of the coupled interaction problem between the fluid flow and the phononic surface presents substantial theoretical and numerical challenges, and is therefore left for future investigation.

3.1.1. *Bloch analysis without fluid interaction*

We first investigate the dynamical properties of the ideal viscoelastic structure displayed in figure 5. As illustrated in figure 5(*a*), this structure is infinitely long in the x direction and clamped at the bottom boundary. It is obtained by periodically repeating in the x direction the unit cell displayed in figure 5(*b*). The height of this unit cell is fixed to $h = 2.35$ mm while its length l_I will be varied. This unit cell is made from two different materials. The matrix (orange) is made with an elastomer characterised by Young's modulus E_s, structural viscosity ν_s and density ρ_s defined before. The circular inclusion (red) of diameter $d_I = 0.94$ mm that is inserted into the middle of this matrix is made from an elastomer of the same density ($\rho_I = \rho_s$) and damping ($D_I = D_s$) but with different Young's modulus E_I, here larger than the matrix's Young's modulus, i.e. $E_I > E_s$.

The solid state is defined by the variable $\boldsymbol{q}'_s = [\boldsymbol{\xi}'_s, \boldsymbol{u}'_s, p'_s]^T$, where $\boldsymbol{\xi}'_s$ is the displacement field, $\boldsymbol{u}'_s = \partial_t \boldsymbol{\xi}'_s$ is the velocity field and p'_s is the pressure field introduced to describe the incompressible structure. They satisfy the viscoelastic equations

$$\rho_s \, \partial_t \, \boldsymbol{u}'_s = \nabla \cdot \left(p'_s \, \boldsymbol{I} + \frac{E(\boldsymbol{x})}{3} \left(\nabla \, \boldsymbol{\xi}'_s + (\nabla \, \boldsymbol{\xi}'_s)^T \right) + \frac{D_s}{2} \left(\nabla \, \boldsymbol{u}'_s + (\nabla \, \boldsymbol{u}'_s)^T \right) \right), \quad (3.1)$$

$$0 = \nabla \cdot \boldsymbol{\xi}'_s, \quad (3.2)$$

where the spatially varying Young's modulus $E(\boldsymbol{x})$ is a l_I-periodic function in the x direction defined as $E(\boldsymbol{x}) = E_s$ for $\boldsymbol{x}$ in the matrix's material and $E(\boldsymbol{x}) = E_I$ for $\boldsymbol{x}$ in the inclusion. The structure is clamped at the bottom boundary at $y = -h = -2.35$ mm, i.e. $\boldsymbol{\xi}'_s = \boldsymbol{u}'_s = \boldsymbol{0}$. Here, we do not consider any interaction with the fluid and therefore impose a stress-free boundary condition at the top $y = 0$, i.e. $\partial_x \xi'_{s,y} + \partial_y \xi'_{s,x} = 0$ and $-p'_s + 2\partial_y \xi'_{s,y} = 0$.

According to Bloch's theorem (Ziman 1972), the waves propagating in this infinitely long x-periodic structure can be represented as a superposition of Bloch waves in the x direction in the form

$$\boldsymbol{q}'_s(\boldsymbol{x}, t) = \int_0^\infty \boldsymbol{q}_s(\boldsymbol{x}, t; \beta_x) \, \mathrm{e}^{\mathrm{i}\beta_x \, x} \, \mathrm{d}\beta_x + \text{c.c.} \quad \text{with} \quad \boldsymbol{q}_s(\boldsymbol{x}, t; \beta_x) = \boldsymbol{q}_s(\boldsymbol{x} + l_I \boldsymbol{e}_x, t; \beta_x).$$

$$(3.3)$$

The complex field $\boldsymbol{q}_s(\boldsymbol{x}, t; \beta_x)$, associated with the wavenumber $\beta_x = 2\pi/\lambda_x$, is l_I-periodic in the x direction, but the wavenumber β_x is a real parameter that allows for the solid perturbation $\boldsymbol{q}'_s(\boldsymbol{x}, t)$ to break this spatial periodicity of the lattice. Without any simplification of the problem, the range of values for β_x can be restricted to the irreducible first Brillouin region, i.e. $-\pi/l_I \leq \beta_x \leq \pi/l_I$ (Brillouin 1946). Moreover, as $\tilde{\boldsymbol{q}}_s(-\beta_x) = \tilde{\boldsymbol{q}}^*_s(\beta_x)$ from the above definition, the investigated range of values can be further reduced to $0 \leq \beta_x \leq \pi/l_I$. The structure being made with viscoelastic material, we further decompose the periodic complex fields as

$$\boldsymbol{q}_s(\boldsymbol{x}, t; \beta_x) = \tilde{\boldsymbol{q}}_s(\boldsymbol{x}; \beta_x)\, \mathrm{e}^{(\gamma - \mathrm{i}\omega)t}, \tag{3.4}$$

where γ and ω represent the temporal growth rate (decay) and frequency of the solid mode $\tilde{\boldsymbol{q}}_s$. Note that the phase and group velocities of the Bloch waves are then classically given by $v_\phi = \omega/\beta_x$ and $v_g = \partial\omega/\partial\beta_x$, respectively. By injecting the decompositions (3.3) and (3.4) into the viscoelastic model (3.1)–(3.2), we obtain the following eigenvalue problem:

$$(\gamma - \mathrm{i}\omega)\,\tilde{\boldsymbol{\xi}}_s = \tilde{\boldsymbol{u}}_s, \tag{3.5}$$

$$(\gamma - \mathrm{i}\omega)\,\tilde{\boldsymbol{u}}_s = \frac{1}{\rho_s}\nabla_\beta \cdot \left(\tilde{p}_s\,\boldsymbol{I} + \frac{E(\boldsymbol{x})}{3}\big(\nabla_\beta\,\tilde{\boldsymbol{\xi}}_s + (\nabla_\beta\,\tilde{\boldsymbol{\xi}}_s)^T\big) + \frac{D_s}{2}\big(\nabla_\beta\,\tilde{\boldsymbol{u}}_s + (\nabla_\beta\,\tilde{\boldsymbol{u}}_s)^T\big) \right), \tag{3.6}$$

$$0 = \nabla_\beta \cdot \tilde{\boldsymbol{\xi}}_s, \tag{3.7}$$

defined in the unit cell shown in figure 5(*b*). Note that the spatial operator has changed and is now defined as $\nabla_\beta = (\partial_x + \mathrm{i}\beta_x, \partial_y)$. As previously defined, zero shear stress and clamped boundary conditions are, respectively, imposed at the top and bottom boundaries of the unit cell. On the left and right boundaries of the unit cell, periodic boundary conditions are finally imposed for all variables, i.e.

$$\tilde{\boldsymbol{q}}_s(-l_I/2, y) = \tilde{\boldsymbol{q}}_s(l_I/2, y). \tag{3.8}$$

The right-hand-side operator in the eigenvalue problem introduced above is invariant by a combination of the spatial transformation $x \to -x$ and the conjugate operation $()^*$. Consequently, the eigenvalue spectrum obtained for a given value of β_x is symmetric with respect to frequency axis ω. For a solid mode $\tilde{\boldsymbol{q}}_s$ associated with the eigenvalue $(\gamma - \mathrm{i}\omega)$ that propagates in the x direction with positive phase velocity $v_\phi = \omega/\beta_x$, we obtain that the complex conjugate solid mode $\tilde{\boldsymbol{q}}^*_s$ associated with the eigenvalue $(\gamma + \mathrm{i}\omega)$ propagates with negative phase velocity $v_\phi = -\omega/\beta_x$. The full eigenvalue spectrum of the infinitely long x-periodic structure illustrated in figure 5(*a*) is finally constructed by repeatedly solving the eigenvalue problem in the unit cell with real wavenumber varying in the range $0 \leq \beta_x \leq \pi/l_I$.

3.1.2. *Bloch analysis with fluid interaction*

We now investigate the dynamical properties of the infinitely long x-periodic structure interacting at its top boundary with the fluid, as shown in figure 6(*a*), that is characterised by density ρ_f and dynamic viscosity μ_f. The fluid–structural unit cell shown in figure 6(*b*) is now composed of the solid unit described in the previous subsection with a fluid column at the top. Unlike the analysis performed in § 2, we simplify the analysis by considering that the fluid is at rest. This analysis allows us to take into account the fluid added mass in the study of the natural dynamics of a solid, as recently addressed by Zhang *et al.* (2024) for a two-dimensional phononic plate.

The flow perturbation is defined by the variable $\boldsymbol{q}'_f = [\boldsymbol{u}'_f, p'_f]^T$, where $\boldsymbol{u}'_f$ is the fluid velocity perturbation and p'_f is the fluid pressure perturbation. Following the two
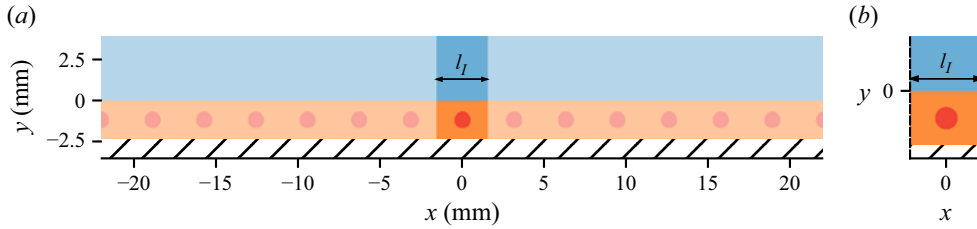
Figure 6. Infinite, periodic, phononic surface interacting with a fluid at rest. The periodic cell (*b*) – clamped at the bottom and interacting with the fluid at the top – with span l_I is periodically and infinitely replicated along the *x* direction (*a*).

decompositions introduced in the previous subsection for the solid perturbation, we decompose the fluid perturbation as

$$q'_f(x, t) = \int_0^\infty \tilde{q}_f(x; \beta_x) \, e^{i(\beta_x x - \omega t)} e^{\gamma t} \, d\beta_x + \text{c.c.} \quad \text{with} \quad \tilde{q}_f(x; \beta_x) = \tilde{q}_f(x + l_I e_x; \beta_x). \tag{3.9}$$

By introducing this decomposition into the Stokes equation governing the fluid perturbation, we obtain

$$(\gamma - i\omega) \, \tilde{u}'_f = \frac{1}{\rho_f} \nabla_\beta \cdot \left(-\tilde{p}'_f I + \mu_f \left(\nabla_\beta \tilde{u}'_f + (\nabla_\beta \tilde{u}'_f)^T \right) \right) \qquad \text{in } \Omega_f, \tag{3.10}$$

$$0 = \nabla_\beta \cdot \tilde{u}'_f \qquad \text{in } \Omega_f, \tag{3.11}$$

where Ω_f denotes here the fluid domain in the unit cell. These fluid equations are coupled at the fluid–solid interface to the solid equations (3.5), (3.6) and (3.7) defined in the solid domain Ω_s. The continuity of the velocity and stress perturbation at the interface $y = 0$ is simply written

$$\tilde{u}'_f = \tilde{u}'_s \qquad \text{on } \Gamma_{fs} \tag{3.12}$$

$$\left(-\tilde{p}'_f I + \mu_f \left(\nabla_\beta \tilde{u}'_f + (\nabla_\beta \tilde{u}'_f)^T \right) \right) (-e_y)$$
$$= \left(\tilde{p}_s \, I + \frac{E(x)}{3} \left(\nabla_\beta \tilde{\xi}_s + (\nabla_\beta \tilde{\xi}_s)^T \right) + \frac{D_s}{2} \left(\nabla_\beta \tilde{u}_s + (\nabla_\beta \tilde{u}_s)^T \right) \right) e_y \qquad \text{on } \Gamma_{fs}. \tag{3.13}$$

Equations (3.12) and (3.13) ensure that the fluid and solid perturbations respect the kinematic and dynamic conditions at the interface. The coupled eigenvalue problem is defined on the fluid–solid unit cell by (3.5), (3.6) and (3.7) coupled to (3.10) and (3.11) through the interface conditions (3.12) and (3.13). Periodic boundary conditions are applied to all variables on the left and right boundaries. At the top boundary of the fluid domain, the stress-free condition is imposed. Finally, the dispersion relation of fluid–solid Bloch waves in this infinitely long *x*-periodic structure interacting with the fluid at rest is obtained by solving this eigenvalue problem for values of the real wavenumber in the range $0 \leq \beta_x \leq \pi/l_I$. Note that the same symmetry argument holds for the Stokes equations, i.e. the fluid–structural mode $(\tilde{q}_f, \tilde{q}_s)$ associated with the eigenvalue $(\gamma - i\omega)$ is related to the complex conjugate mode $(\tilde{q}_f^*, \tilde{q}_s^*)$ associated with the eigenvalue $(\gamma + i\omega)$, with the two modes propagating with the same velocity but in opposite directions.

3.2. *Results of Bloch analyses*

Results of the Bloch analyses are first presented for the infinitely long phononic compliant surface with geometrical and material properties similar to those of the finite-length phononic compliant surface described in the previous section (§ 2). The dispersion relation and modes are described for the case without fluid interaction in § 3.2.1 and with interaction with a fluid at rest in § 3.2.2. The effect of the inclusion's spacing l_I and Young's modulus E_I on the frequency band gap is then investigated in § 3.2.3.

3.2.1. *Infinitely long phononic compliant surface without fluid interaction*

Figure 7 presents the eigenvalues computed for the infinitely long periodic structure, with $l_I = 2.35$ mm and $E_I = 10E_s$ and without fluid interaction. These parameters correspond to the phononic compliant surface studied in § 2. In the top-left panel, the frequencies $f = \omega/2\pi$ associated with the identified eigenvalue branches are plotted as a function of the wavenumber β_x. These same branches are also visible in the eigenvalue spectrum shown in the top-right panel, where the frequency is plotted against the normalised growth ratio γ/ω. All eigenvalues exhibit negative damping due to the intrinsic viscous properties of the materials, leading to natural solid waves whose amplitudes decay over time. For $f \geq 600$ Hz, the frequency axis is not continuously populated, revealing the presence of band gaps between the identified branches (highlighted in red areas). Within these band gaps, only evanescent waves can propagate, effectively preventing long-range energy transport.

The eigenmode of the lowest-frequency branch corresponding to $\beta_x = \pi/(2l_I)$ is displayed in figure 7(*a*). In the left-hand panel, the vertical component of the displacement perturbation field is displayed with colours at the (arbitrary) instant $t = 0$. This mode is shown on a domain composed of 10 unit cells (inclusions) for visualisation purposes, but was computed on a single unit cell. The displacement at the top boundary is also displayed with arrows. In the right-hand panel, the vertical displacement of the interface is shown as a function of space x and time t. This Bloch mode is characterised by a spatially periodic pattern (colour) modulated by the wavelength $2\pi/\beta_x = 4 l_I$ of the envelope that is clearly visible at the interface. As can be seen from the right-hand panel, this is a travelling wave propagating along the x direction with a positive phase velocity $v_\phi = \omega/\beta_x$ and a positive group velocity $v_g = \partial\omega/\partial\beta_x$. Note that the complex conjugate eigenmode (obtained for the same value of β_x) provides a Bloch wave travelling in the opposite direction with negative phase and group velocities. When increasing the wavenumber on this low-frequency branch, the group velocity corresponding to the speed of the envelope decreases. At $\beta_x = \pi/l_I$, this group velocity is zero and the envelope of the Bloch mode is a standing wave. The corresponding mode is displayed in figure 7(*b*). Inside the standing-wave envelope of wavelength equal to $2l_I$, a spatially periodic wave propagates with positive phase velocity equal to $v_\phi = 2f_{min}l_I$, where f_{min} is the lowest frequency of the first band gap. As seen in the left-hand panel, the maximal and minimal displacements of the interface are reached in between the inclusions (circles). The Bloch mode displayed in figure 7(*c*) corresponds to the highest frequency f_{max} of the first band gap. This mode is also characterised by a standing-wave envelope of wavelength $2l_I$ but for a larger phase velocity now equal to $v_\phi = 2f_{max}l_I$. The maximal and minimal displacements of the interface are now reached above the inclusions. For frequencies $f_{min} \leq f \leq f_{max}$ in between these two standing Bloch waves, no wave may propagate, thus confirming the wave-blocking properties of the phononic surface along the x direction.

The wavelength $2l_I$ of these two standing Bloch modes occurring at the edges of the band gap is similar to that of the TWF instability, as observed in figure 2. This establishes the first principle for designing our phononic surface: its spatial periodicity should be half
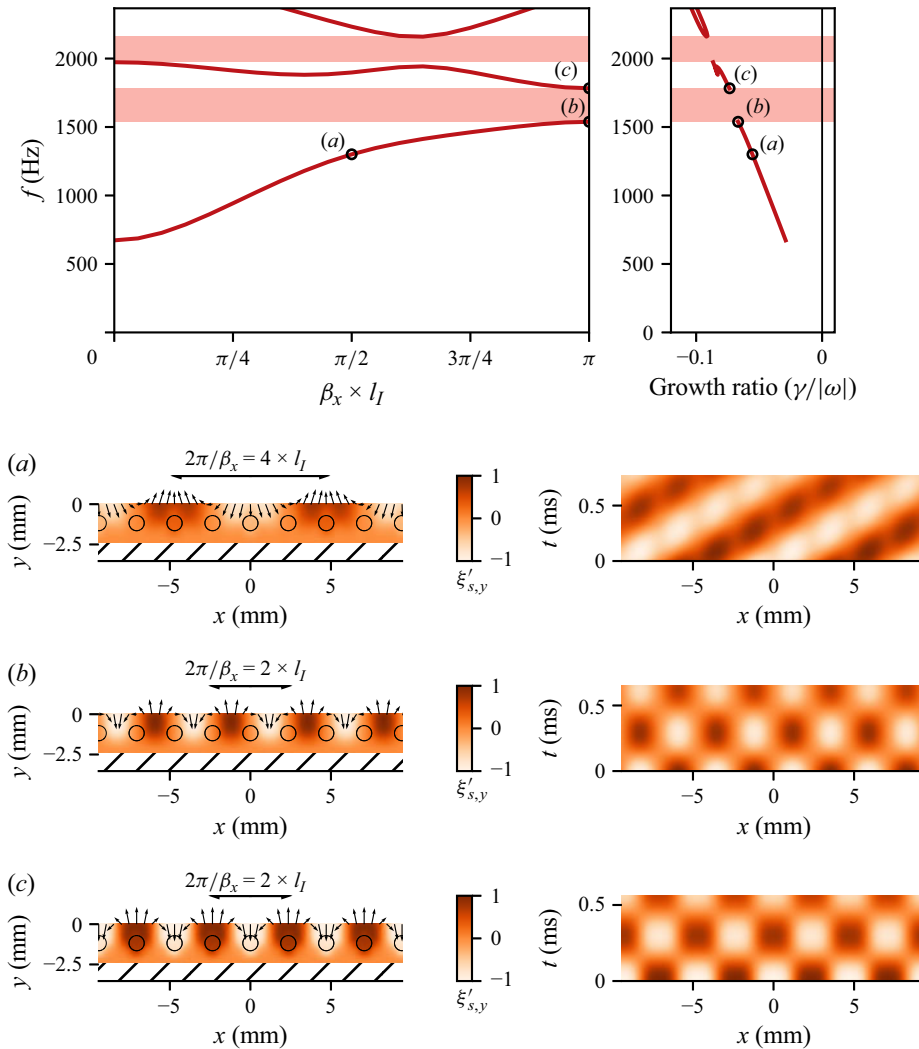
Figure 7. (Top) Dispersion relation from Bloch analysis for an isolated, x-periodic phononic medium. The shaded red areas highlight the bands of angular frequencies for which no eigenvalues are found (band gaps). (a–c) The time–space evolution of the modes labelled in the top figures. On the left, the colour map reports the vertical displacement field in the solid domain at $t = 0$, while the vectors the displacement at the interface. On the right, the colour map reports time–space evolution of the vertical displacement at the interface over one oscillation.

of the wavelength of the TWF wave to control. The second principle is that the bang-gap frequency also matches the range of frequency where TWF instabilities are amplified. The frequency band gap predicted by the present Bloch analysis extends in the range $1540\,\text{Hz} \le f \le 1780\,\text{Hz}$, while that observed for the finite-length phononic surface in § 2.3 sits between 1241 and 1439 Hz. We anticipate that this overestimation of the frequency band gap is mainly due to the interaction of the compliant surface with a heavy fluid (water). Added-mass effects can then significantly alter the frequencies of the natural vibration modes of structures (Pfister & Marquet 2020) and should be taken into account to design the phononic compliant surface.
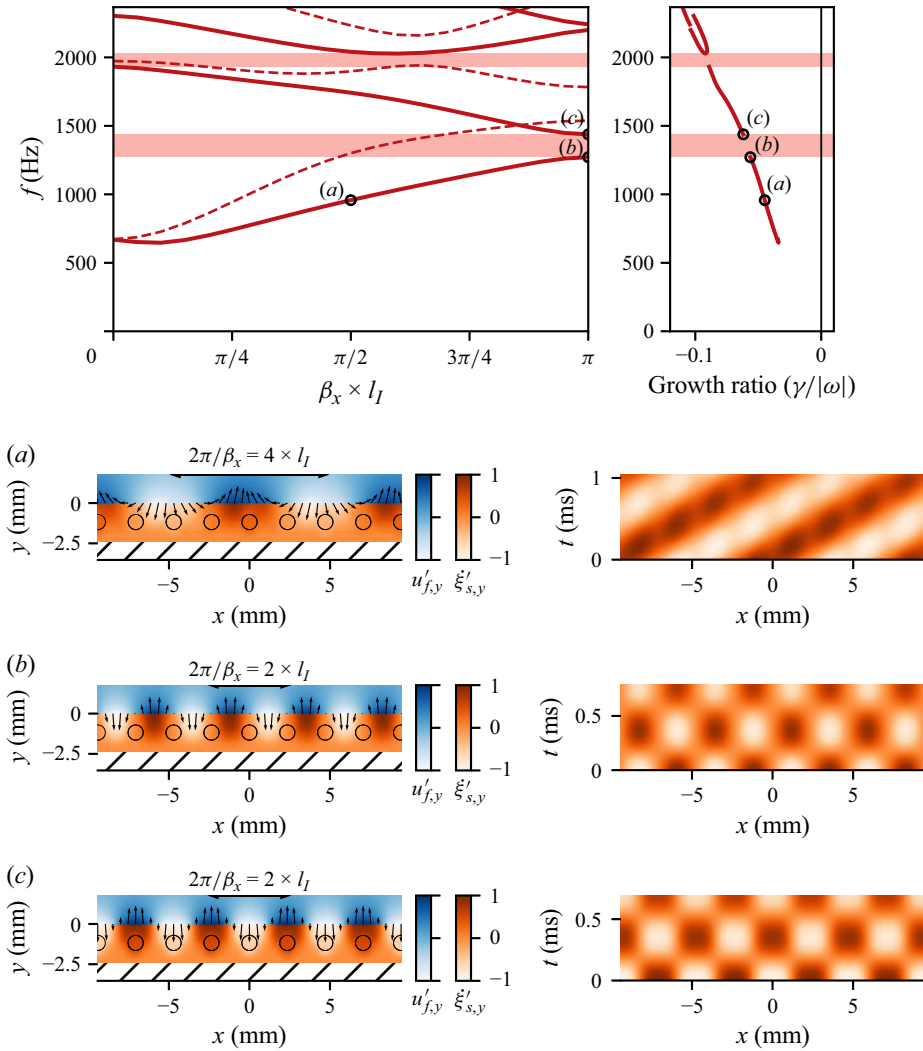
Figure 8. Dispersion relation from Bloch analysis for a viscoelastic, periodic solid interacting with a fluid at rest (solid lines). The shaded areas highlight the bands of angular frequencies for which no eigenvalues are found (band gaps). The dashed lines report the dispersion relation for the isolated periodic solid (see figure 7). (*a*–*c*) The modal shapes of the modes labelled in the top figures. On the left, the colour maps report the vertical displacement field in the solid (orange) and fluid (blue) domains at $t = 0$, while the vectors the displacement at the interface. On the right, the time–space evolution of the vertical displacement at the interface is reported over one oscillation.

3.2.2. *Infinitely long phononic compliant surface with fluid interaction*

To capture the added-mass effect of the heavy fluid (water) on the frequencies of the Bloch modes, we now present results of the Bloch analysis for an infinitely long phononic compliant structure that interacts with a still fluid as discussed in §3.1.2. Figure 8 displays with solid curves the branch of eigenvalues computed with the coupled fluid–solid eigenvalue problem, while dashed curves correspond to the original one. The branches are modified and the expected shift towards lower frequency is observed. The first band gap now sits in the range 1270 Hz $\leq f \leq$ 1440 Hz, to be compared with 1241 Hz $\leq f \leq$ 1439 Hz from the global stability analysis of the finite-length phononic surface in §2.3.
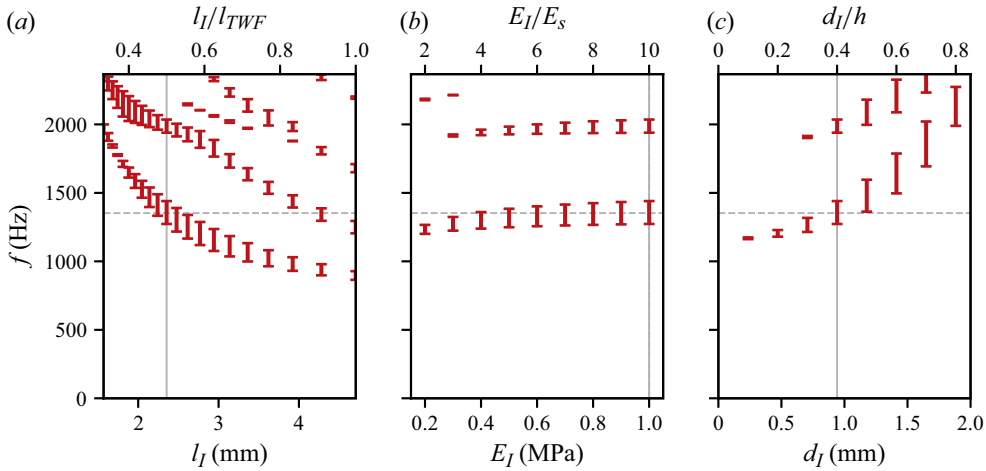
Figure 9. Parametric study on the spacing l_I (a), Young's modulus E_I (b) and diameter d_I (c) of the inserts. The error bars indicate the location of the band gaps at each computed point. The data in (a) are for $E_I = 10E_s$, $d_I = 0.94$ mm and varying l_I; those in (b) for $l_I = 2.35$ mm, $d_I = 0.94$ mm and varying E_I; those in (c) for $E_I = 10E_s$, $l_I = 2.35$ mm and varying d_I. The vertical grey lines indicate the design point, reported in figure 8. The horizontal dashed grey lines indicate the frequency at which the TWF peak occurs.

Additionally, the frequency range of the band gap in the phononic compliant surface is now in much better agreement with the targeted value $f = 1350$ Hz, at which the maximal amplification of TWF occurs. The agreement also validates the general principle of the present phononic compliant surface that is to forbid the propagation of the solid waves in the range of frequencies where TWF is most amplified. From the right-hand panel, a slight increase in the growth ratio is also noted. Looking at the shapes of the modes limiting the band gap (figure 8a,b), they present the same structure as those identified for the isolated solid (figure 7a,b). When the interface vibrates, it drives the fluid in its upward/downward motion, which means the solid has to displace the mass of the fluid, which qualitatively explains the lower natural frequency. In the case considered, this effect is important since the mass ratio between the solid (elastomer) and the fluid (water) is unitary; in air, it would be less pronounced because of the lower density of the fluid.

3.2.3. *Effect of inclusion spacing, Young's modulus and diameter on frequency band gaps*

The results previously reported have been obtained for unit cells of size $l_I = 2.35$ mm $\approx l_{TWF}/2$ and Young's modulus $E_I = 1$ MPa $= 10E_s$ that lead to the attenuation of the TWF reported in the first section. We now investigate the impact of these two parameters on the positioning and extent in frequency of the band gaps in relation to the TWF amplification peak, providing a comprehensive explanation for the choice of the selected design point.

Figure 9(a) presents a parametric investigation into the effect of insert spacing l_I on the dynamic behaviour of the phononic compliant surface interacting with the still fluid, for insert rigidity $E_I = 1$ MPa. The error bars in this figure represent the frequency range delimiting the band gaps that is displayed as a function of the dimensional value of l_I (bottom axis) and the non-dimensional value l_I/l_{TWF} (top axis) where l_{TWF} is the wavelength of TWF instabilities for $f = 1350$ Hz (horizontal dashed line). The design point explored so far is highlighted by the vertical solid line at $l_I = 2.35$ mm $\approx l_{TWF}/2$. For this spacing, the first band gap is centred at the target frequency and wavelength of the TWF waves, thus confirming again the successful design based on Bloch analysis.

Increasing the spacing l_I is observed to shift the band gaps towards lower frequencies. For the first band gap (lowest frequency), this phenomenon can be explained by recalling that the limiting frequencies correspond to Bloch modes of two different branches occurring at wavenumber $\beta_x = \pi/l_I$ (see figure 8). As l_I decreases, the wavenumber of the limiting Bloch modes thus increases and consequently the frequencies delimiting the bang gap also increase. Conversely, increasing the spacing l_I leads to lower wavenumbers, resulting in lower frequencies. This general trend is also observed for the second band. Interestingly, its frequency range is centred around the targeted frequency of TWF for $l_I = 4.28$ mm, suggesting that the TWF may also be attenuated with this new compliant phononic surface. As the bang gap is narrower than for $l_I = 2.35$ mm, we may also anticipate that its effect is more limited.

Once the inserts' spacing l_I is fixed, their rigidity can be exploited to pilot the extension of the band gap. This effect is illustrated in figure 9(*b*) where band gaps are reported for a varying Young's modulus E_I of the insert material, while the spacing is fixed at $l_I = 2.35$ mm $\approx l_{TWF}/2$. As before, the horizontal dashed line indicates the target frequency and the vertical solid line the chosen design point, i.e. $E_I = 1$ MPa $= 10E_s$, where E_s is the Young's modulus of the material surrounding the insert. The width and location of the band gap stabilise for $E_I > 0.8$ MPa and no significantly different behaviour is observed at higher values than the design one. For lower values, instead, the band gap shrinks and shifts to lower frequency. At $E_I = 0.1$ MPa $= E_s$, no band gaps are observed, the case being equivalent to a homogeneous surface.

This study employs a simple circular geometry for the scatterer, chosen arbitrarily to illustrate the fundamental principle behind using phononic surfaces to suppress TWF. Up to this point, the scatterer's diameter (d_I) has been set to 0.94 mm, balancing between the overall wall compliance and the band-gap size. Figure 9(*c*) presents the location of band gaps as a function of scatterer diameter (d_I), with fixed parameters $l_I = 2.35$ mm and $E_I = 1$ MPa. At the design point ($d_I = 0.94$ mm $= 0.4\,h$), the band gap is centred at the target frequency corresponding to TWF. As the diameter increases, the band gaps widen but also shift towards higher frequencies due to the stiffening effect caused by the increasing proportion within the unit cell of the space occupied by the stiffer material making the scatterer. Notably, a stiffer structure would lead to a reduced attenuation of the TSW, as documented in Pfister *et al.* (2022); therefore, if a geometrical optimisation of the shape of the scatterers is performed, a constraint should be considered to take into account this effect.

3.3. *Comparison with eigenvalue analyses of finite-length phononic compliant surfaces*

Thus far, this section has outlined the design process for the unitary cell of the phononic surface using Bloch analysis, with the primary objective of suppressing the propagation of waves responsible for TWF. This analysis is based on the assumption of an infinitely extended surface; in the following, this hypothesis is dropped and the dynamics of a finite phononic surface is compared with the results of the Bloch analysis.

The coupled interaction of a finite patch with a flow at rest is considered. The eigenvalue problem (2.3) is considered with a vanishing base solution $Q = 0$: the velocity of the base flow is zero ($U_f(x) = 0$) as well as the displacement of the structure, i.e. $\Xi_s(x) = 0$, in order to be consistent with the analysis in § 3.2.2 for the infinite plate interacting with a fluid at rest. Note that, in the absence of fluid flow, the concept of a Reynolds number derived from boundary-layer characteristics becomes inapplicable. However, for consistency, the fluid's viscosity remains identical to that of water used in previous analyses. Figure 10 presents a comparative analysis of eigenvalues obtained for the
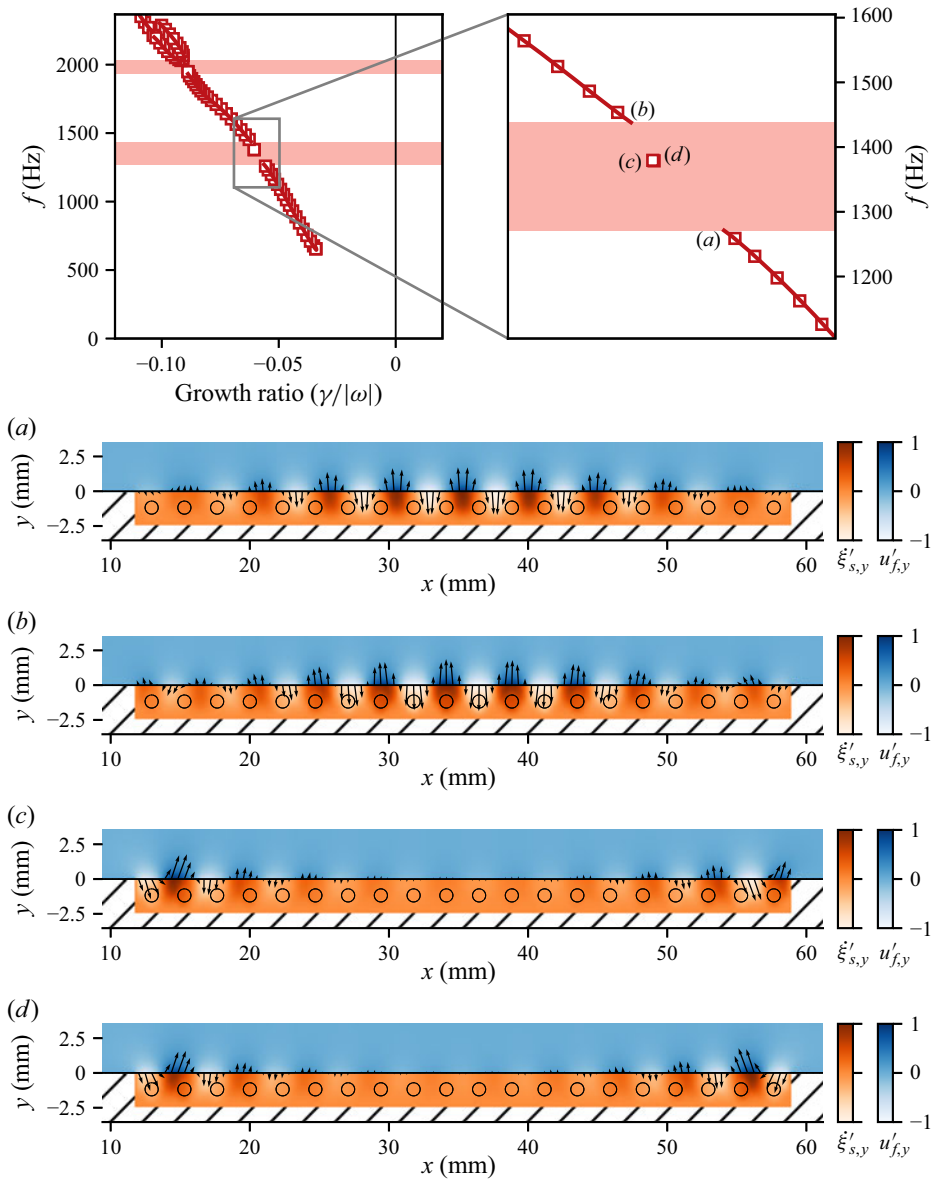
Figure 10. Comparison between the fluid–structural eigenvalue branches computed by means of the Bloch analysis (lines, see figure 8) and the eigenvalues of the finite-length surface (squares). A fluid at rest is considered for the two analyses. The coloured shaded areas indicate the band gaps predicted by the Bloch analysis. (*a–d*) The respective modal shapes of the modes labelled in the top figure (for a finite-length structure).

finite-length phononic surface (red squares) and from the Bloch analysis of the infinite-length phononic surface (red lines), revealing both similarities and key differences. The primary distinction stems from the discrete nature of the eigenvalues in the finite-length case, as opposed to the continuous branches predicted by the Bloch analysis – an expected outcome due to the finite spatial extent of the surface. Despite this, the discrete eigenvalues lie precisely on the continuous branches, demonstrating that the Bloch analysis reliably predicts both frequency and damping characteristics of the finite-length surface.

Regarding modal shapes, figures 10(*a*) and 10(*b*) show the eigenmodes near the first band gap, as indicated in the top panel of the figure. These modes exhibit a structure consistent with those predicted by the Bloch analysis: in particular, they feature surface oscillations occurring between the inserts (figure 10*a* versus figure 8*b*) and above the inserts (figure 10*b* versus figure 8*c*). An amplitude modulation along the *x* direction is observed, which is attributed to the lateral clamped boundary conditions imposed on the finite-length phononic surface. A second notable difference with respect to the Bloch analysis is the appearance of a double eigenvalue within the band gap, referred to as truncation resonance (Rosa *et al.* 2023). This phenomenon arises from the breaking of periodicity induced by the finite length of the surface and the clamped boundary conditions at its lateral ends. These eigenmodes shown in figures 10(*c*) and 10(*d*) are spatially localised near the left and right boundaries of the surface. One exhibits a symmetric structure, while the other is anti-symmetric. Importantly, both mode share the same eigenvalue, which implies that they can be linearly combined to form spatial structures fully localised at either boundary, while still satisfying the coupled eigenvalue problem for the same eigenvalue. These truncation modes also appear when the compliant phononic surface interacts with the boundary-layer flow (§ 2.3). In this configuration, the fluid is no longer at rest; instead a boundary layer develops over the surface. Two isolated eigenmodes are observed at close frequencies ($f = 1343$ Hz and $f = 1347$ Hz; see figure 2*b*) each localised near one of the lateral boundaries (see figure 3). Unlike in the static fluid case, where symmetric and anti-symmetric pairs of eigenmodes are found, the base flow velocity oriented in the streamwise direction breaks the symmetry and yields two distinct, localised modes. The slight frequency difference between the two modes ($f = 1343$ Hz versus $f = 1347$ Hz) is likely due to the streamwise development of the boundary layer, which interacts differently with the compliant surface at the upstream and downstream edges.

Beyond the isolated truncation modes, the proposed fluid–structure Bloch analysis accurately captures the frequency range of the band gaps, a key feature for the effective suppression of TWF. This is clearly demonstrated by the strong agreement between the predicted band gap from the Bloch analysis (1270 Hz $\leq f \leq 1440$ Hz) and the observed band gap for the finite-length phononic surface (1241 Hz $\leq f \leq 1439$ Hz). This close correspondence underscores the reliability of the Bloch framework as a predictive and practical design tool for compliant phononic surfaces aimed at TWF control, even when applied to finite-length configurations.

4. Conclusions

This study builds upon the previous work by Pfister *et al.* (2022), which investigated the attenuation of TSWs in a boundary-layer flow by means of a wall-mounted, conventional compliant surface of finite length and made of a homogeneous, viscoelastic material. Their findings reveal that, alongside the desired attenuation of TSWs, a further disturbance amplification peak emerges. This peak is related to the fluid–structural interaction of the compliant surface with the flow, known in the literature as TWF (Carpenter & Garrad 1986).

In the present study, we successfully addressed the suppression of this secondary peak by introducing periodic stiff inserts into the solid, thereby creating a phononic compliant surface oriented along the streamwise direction (§ 2). Phononic metamaterials can selectively block wave propagation in solids within specific frequency and wavelength bands. Although their application in TSW passive control is not novel (e.g. Kianfar & Hussein 2023; Michelis *et al.* 2023), to our knowledge, this work marks the first use

of phononic surfaces to attenuate TWF or, more generally, a fluid–structural instability. Global stability analysis of the coupled system demonstrates that the phononic compliant surface attenuates the TWF peak while maintaining also the attenuation of TSWs. The latter persist, as for the conventional compliant surface, also downstream of the compliant wall (§ 2.3). In general, this is not the case when the localised interaction of phononic subsurfaces and the fluid is used to attenuate TSWs. In these studies, a localised increase in amplitude at the trailing edge of the compliant surface results in an overall amplification of the TSWs (Michelis *et al.* 2023), even if recent studies suggest that patterns of localised phononic subsurfaces may mitigate this issue (Hussein *et al.* 2025). Overall, the current configuration featuring a streamwise-extended phononic surface remains very promising for the attenuation of TSWs, while avoiding the amplification of TWF.

In order to provide a better insight in the design choices that led to the attenuation mechanism of TWF, we introduced a Bloch analysis of a streamwise-infinite phononic surface (§ 3). First, we considered an isolated periodic elastic body without fluid and with a stress-free boundary condition at the top (§ 3.2.1). The blocked wave's wavelength was accurately predicted, but not its frequency due to the absence of fluid. In order to be predictive of both wavelength and frequency of the blocked waves, the added mass of the fluid was also taken into account by considering a fluid at rest over the phononic medium (§ 3.2.2). This analysis allowed us to validate the design principle that the periodicity along the controlled-wave direction (i.e. the streamwise direction) should match half of its wavelength (§ 3.2.3). A comparative assessment with global stability analysis for a finite phononic surface of equivalent design validated the predictive capability of the Bloch analysis results, capturing the dynamic behaviour exhibited by the installed phononic compliant wall (§ 3.3).

4.1. *Perspectives*

The introduced fluid–structural Bloch framework could be directly extended to incorporate non-zero base-flow conditions, provided that the fluid's periodicity aligns with the unitary cell or, alternatively, a common periodic framework is established within the coupled system. A pertinent example of applying this principle to a fluid-only problem can be found in Jouin, Robinet & Cherubini (2024), where the authors employed the Bloch formalism, as introduced by Schmid, de Pando & Peake (2017), to investigate the stability of spanwise-periodic channel flows. However, the focus on zero-pressure-gradient boundary-layer flow of the current study presents a notable exception. Specifically, this type of flow exhibits spatial inhomogeneity along the streamwise direction, characterised by a boundary-layer thickness that monotonically increases with the streamwise coordinate (Batchelor 2000). This leads to the absence of periodicity along the streamwise direction and, thus, does not allow for a direct extension of the presented formalism to the interaction of a phononic surface with a zero-pressure-gradient boundary-layer flow.

In this study we explored the linear dynamic of the coupled fluid–structural system, given by the boundary-layer flow and the phononic compliant surface. Under the hypothesis of linearity, we showed that TSWs are attenuated and TWF is suppressed. However, this represents only the initial step towards the application of this control technique to delaying the laminar-to-turbulent transition in the flow. Linear studies, as the current one, call for further inquiries towards the assessment of the transition delay; this could come from either a numerical or experimental standpoint. The former would require the development of three-dimensional numerical frameworks to perform time-resolved, nonlinear simulations of the fluid–structural coupling. The latter would involve modern fabrication techniques, such as three-dimensional printing or polymer lithography, for the

realisation of the compliant phononic surface; moreover, if water is considered as a fluid, the here-specified flow condition could be achievable, for instance, in a towing tank.

The findings of the current study are limited to a simple unitary periodic cell geometry, comprising a stiff circular scatterer embedded within a homogeneous flexible matrix. Further developments could involve more complex geometries, such as those presented in Park *et al.* (2022), the integration of local resonators, as discussed in Kianfar & Hussein (2023), or geometry optimisation in order to achieve finer control over the band-gap positions and widths within the frequency domain. Nevertheless, despite its simplicity, the chosen geometry has successfully served as a proof of concept for the underlying design principle, validating its potential for further development and optimisation. The present results can facilitate the effective use of compliant surfaces for TSW attenuation, subsequently delaying the laminar-to-turbulent transition, by addressing one of the primary constraints: the premature transition triggered by TWF (Lucey & Carpenter 1995).

The present proof of concept could inspire further research aimed at enhancing the performance of these surfaces as presented here, and/or applying phononic surfaces to address other fluid–structural problems where wave propagation in the solid phase serves as one of the driving mechanisms. Notably, the results presented herein pertain to water flow, benefiting from a unity density ratio between the solid and fluid phases. However, a critical challenge remains in adapting these techniques for aerodynamic flows, where the substantial increase in density ratio introduces complexity. Despite this, a promising application lies in supersonic flows (Zhao *et al.* 2019; Klauss *et al.* 2025), where elevated velocities might compensate for lower fluid densities.

Declaration of interests. The authors report no conflict of interest.

Appendix A. Arbitrary Lagrangian–Eulerian formulation of the fluid–structural problem

This appendix presents a summary of the formulation introduced in Pfister *et al.* (2019), based on the ALE formulation of the fluid–structural problem and here used to model the coupled dynamics of the fluid and solid phases. We refer the reader to Pfister (2019) and Pfister *et al.* (2019, 2022) for further details.

The fluid state – composed of fluid velocity u_f and pressure p_f – is augmented to include the operator ξ_e that maps the fluid equations – naturally expressed in the deformed domain – to the fixed reference fluid domain Ω_f. The resulting equation for the fluid phase reads

$$\rho_f \, J(\xi_e) \, \partial_t u_f = -\rho_f \left(\nabla u_f \boldsymbol{\Phi}(\xi_e) \right) \left(u_f - \dot{\xi}_e \right) + \nabla \cdot \boldsymbol{\Sigma}_f(u_f, p_f, \xi_e; \mu_f) + f \quad \text{in } \Omega_f, \tag{A1}$$

$$0 = \nabla \cdot \left(\boldsymbol{\Phi}(\xi_e) \, u_f \right) \qquad \qquad \text{in } \Omega_f, \tag{A2}$$

where $\boldsymbol{\Sigma}_f$ is the fluid stress tensor, mapped to the reference domain. The extension operator ξ_e enters in the formulation via the deformation operator $\boldsymbol{\Phi}(\xi_e) = J(\xi_e) \boldsymbol{F}^{-1}(\xi_e)$, with $\boldsymbol{F}(\xi_e) = \boldsymbol{I} + \nabla \xi_e$ and $J(\xi_e) = \det(\boldsymbol{F}(\xi_e))$. Since the particular form of the extension

operator is arbitrary, a Laplace equation is used here. A volume forcing $f(x, t)$ is also introduced in the fluid domain Ω_f, to later study the forced response of the system. The solid equations, instead, are written in the solid domain Ω_s in their natural Lagrangian form:

$$\rho_s \, \partial_t^2 \boldsymbol{\xi}_s = \nabla \cdot \boldsymbol{P}_s(\boldsymbol{\xi}_s, \dot{\boldsymbol{\xi}}_s, p_s; E_s, D_s) \qquad \text{in } \Omega_s, \qquad \text{(A3)}$$

$$0 = \nabla \cdot \boldsymbol{\xi}_s \qquad \text{in } \Omega_s, \qquad \text{(A4)}$$

where $\boldsymbol{\xi}_s$ is the displacement vector of the solid and p_s the isotropic part of the solid stress tensor $\boldsymbol{P}_s$. The continuity of stress and displacement along the fluid–structural interface Γ_{fs} is ensured by imposing the following conditions:

$$\boldsymbol{\xi}_e = \boldsymbol{\xi}_s \qquad \text{on } \Gamma_{fs}, \qquad \text{(A5)}$$

$$\boldsymbol{\Sigma}_f \, \boldsymbol{n} = \boldsymbol{P}_s \, \boldsymbol{n} \qquad \text{on } \Gamma_{fs}. \qquad \text{(A6)}$$

Dirichlet boundary conditions are enforced on the complete fluid velocity vector $\boldsymbol{u}_f$ at the rigid-wall ($\Gamma_{f,w}$) and inflow ($\Gamma_{f,i}$) boundaries, while only the streamwise component is prescribed at the free stream ($\Gamma_{f,\infty}$):

$$\boldsymbol{u}_f = \boldsymbol{0} \qquad \text{on } \Gamma_{f,w}, \qquad \text{(A7)}$$

$$\boldsymbol{u}_f = \boldsymbol{u}_{Blasius} \qquad \text{on } \Gamma_{f,i}, \qquad \text{(A8)}$$

$$\boldsymbol{u}_{f,x} = U_{f,\infty} \qquad \text{on } \Gamma_{f,\infty}, \qquad \text{(A9)}$$

where $\boldsymbol{u}_{Blasius}$ is the Blasius solution of a boundary-layer flow at the inlet for a free-stream velocity $U_{f,\infty}$. Natural stress-free conditions are considered at the outflow. Regarding the solid phase, a zero displacement is considered along the clamped boundary $\Gamma_{s,c}$:

$$\boldsymbol{\xi}_s = \boldsymbol{0} \qquad \text{on } \Gamma_{s,c}. \qquad \text{(A10)}$$

The complete state q of the coupled fluid–structural system reads as follows:

$$\boldsymbol{q}(x, t) = \begin{bmatrix} \boldsymbol{q}_f(x, t) \\ \boldsymbol{q}_s(x, t) \end{bmatrix} = \begin{bmatrix} \boldsymbol{u}_f(x, t) & p_f(x, t) & \boldsymbol{\xi}_e(x, t) \end{bmatrix} \boldsymbol{\xi}_s(x, t) \quad \dot{\boldsymbol{\xi}}_s(x, t) \quad p_s(x, t) \end{bmatrix}^T,$$
(A11)

where $\boldsymbol{q}_f$ is the fluid state and $\boldsymbol{q}_s$ the solid one. The former is composed of the fluid velocity $\boldsymbol{u}_f$, the fluid pressure p_f and the extension operator $\boldsymbol{\xi}_e$, which maps the fluid quantities from the deformed to the reference domain. The latter is composed of the solid deformation $\boldsymbol{\xi}$, the solid velocity $\dot{\boldsymbol{\xi}}$ and the solid pressure $p_s(x, t)$, i.e. the isotropic part of the solid stress tensor.

The equations introduced above – describing the coupled fluid–structural model – are discretised by means of the finite-element method. The resulting numerical model – as well as the Bloch extension in § 3.1 – is implemented by means of the Python-interfaced, finite-element library DOLFINx (Baratta *et al.* 2023).

The global stability and resolvent analyses in § 2.2 are based on the hypothesis of small perturbations with respect to the steady solution of the coupled ALE formulation presented above. Therefore, the following decomposition is introduced:

$$\boldsymbol{q}(x, t) = \boldsymbol{Q}(x) + \epsilon \, \boldsymbol{q}'(x, t), \qquad \text{(A12)}$$

$$\boldsymbol{f}(x, t) = \epsilon \, \boldsymbol{f}'(x, t),$$

where $\boldsymbol{q}(x, t)$ is the complete state, $\boldsymbol{Q}(x) = [\boldsymbol{U}_f(x), \ P_f(x), \ \boldsymbol{\Xi}_e(x), \ \boldsymbol{\Xi}_s(x), \ P_s(x)]^T$ the steady solution and $\boldsymbol{q}'(x, t)$ the state perturbation, which is multiplied by an arbitrarily small coefficient $\epsilon \ll 1$. The volume forcing $\boldsymbol{f}(x, t)$ is similarly decomposed, with a zero steady contribution, i.e. no steady forcing. By injecting the decomposition (A12) in the

governing equations, the linear equations describing the dynamics of $\boldsymbol{q}'$ are found:

$$
\underbrace{\begin{bmatrix} \boldsymbol{B}_f(\boldsymbol{\Xi}_e) & 0 \\ 0 & \boldsymbol{B}_s \end{bmatrix}}_{\boldsymbol{B}(\boldsymbol{\Xi}_e)} \underbrace{\frac{\partial}{\partial t} \begin{bmatrix} \boldsymbol{q}'_f \\ \boldsymbol{q}'_s \end{bmatrix}}_{\frac{\partial \boldsymbol{q}'}{\partial t}} - \underbrace{\begin{bmatrix} \boldsymbol{A}_f(\boldsymbol{U}_f, \boldsymbol{\Xi}_e) & \boldsymbol{C}_{fs} \\ \boldsymbol{C}_{sf} & \boldsymbol{A}_s \end{bmatrix}}_{\boldsymbol{A}(\boldsymbol{U}_f, \boldsymbol{\Xi}_e)} \underbrace{\begin{bmatrix} \boldsymbol{q}'_f \\ \boldsymbol{q}'_s \end{bmatrix}}_{\boldsymbol{q}'} = \underbrace{\begin{bmatrix} \boldsymbol{P}_f \\ 0 \end{bmatrix}}_{\boldsymbol{P}} \boldsymbol{f}'
$$

$$
\Rightarrow \quad \boldsymbol{B}(\boldsymbol{\Xi}_e) \frac{\partial \boldsymbol{q}'}{\partial t} - \boldsymbol{A}(\boldsymbol{U}_f, \boldsymbol{\Xi}_e) \, \boldsymbol{q}' = \boldsymbol{P}\boldsymbol{f}'.
$$
(A13)

The mass matrix $\boldsymbol{B}$ is related to the inertia of the coupled system: it is diagonal by blocks with one contribution from the fluid $\boldsymbol{B}_f$ and one from the solid $\boldsymbol{B}_s$. The Jacobian matrix $\boldsymbol{A}$, instead, describes the response of the coupled fluid–structural system to small perturbations. The inherent dynamics of flow and structure are captured by $\boldsymbol{A}_f$ and $\boldsymbol{A}_s$, respectively, with coupling enforced at the fluid–solid interface through $\boldsymbol{C}_{fs}$ and $\boldsymbol{C}_{sf}$. Both $\boldsymbol{B}$ and $\boldsymbol{A}$ depend on the base solution $\boldsymbol{Q}$ via two of its components, namely the flow field $\boldsymbol{U}_f$ and the extension field $\boldsymbol{\Xi}_e$. Finally, the forcing operator $\boldsymbol{P}$ restricts the application of the volume forcing $\boldsymbol{f}'$ to the fluid phase. The here-presented linearised operators are assembled by means of the automatic differentiation capabilities of the library DOLFINx (Baratta *et al.* 2023). The eigenvalue problems – for the global stability, resolvent and Bloch analyses – are solved by means of the linear-algebra library SLEPc (Roman *et al.* 2023).

REFERENCES

ASHBY, M.F. 1999 *Materials Selection in Mechanical Design*. Elsevier Science & Technology Books.

BARATTA, I.A., DEAN, J.P., DOKKEN, J.S., HABERA, M., HALE, J.S., RICHARDSON, C.N., ROGNES, M.E., SCROGGS, M.W., SIME, N. & WELLS, G.N. 2023 DOLFINx: The Next Generation FEniCS Problem Solving Environment. Zenodo. https://doi.org/10.5281/zenodo.10447666.

BATCHELOR, G.K. 2000 *An Introduction to Fluid Dynamics*. Cambridge Mathematical Library. Cambridge University Press.

BENJAMIN, T.B. 1960 Effects of a flexible boundary on hydrodynamic stability. *J. Fluid Mech.* **9** (4), 513–532.

BENJAMIN, T.B. 1963 The threefold classification of unstable disturbances in flexible surfaces bounding inviscid flows. *J. Fluid Mech.* **16** (3), 436–450.

BRANDT, L., SIPP, D., PRALITS, J.O. & MARQUET, O. 2011 Effect of base-flow variation in noise amplifiers: the flat-plate boundary layer. *J. Fluid Mech.* **687**, 503–528.

BRILLOUIN, L.N. 1946 *Wave propagation in periodic structures: electric filters and crystal lattices*. In *International Series in Pure and Applied Physics*. McGraw-Hill.

BRUNET, T., LENG, J. & MONDAIN-MONVAL, O. 2013 Soft acoustic metamaterials. *Science* **342** (6156), 323–324.

CARPENTER, P.W. & GARRAD, A.D. 1985 The hydrodynamic stability of flow over Kramer-type compliant surfaces. Part 1. Tollmien-Schlichting instabilities. *J. Fluid Mech.* **155**, 465–510.

CARPENTER, P.W. & GARRAD, A.D. 1986 The hydrodynamic stability of flow over Kramer-type compliant surfaces. Part 2. Flow-induced surface instabilities. *J. Fluid Mech.* **170**, 199–232.

CARPENTER, P.W., LUCEY, A.D. & DAVIES, C. 2001 Progress on the use of compliant walls for laminar-flow control. *J. Aircraft* **38** (3), 504–512.

COLLET, M., OUISSE, M., RUZZENE, M. & ICHCHOU, M.N. 2011 Floquet–Bloch decomposition for the computation of dispersion of two-dimensional periodic, damped mechanical systems. *Intl J. Solids Struct.* **48** (20), 2837–2848.

COLOMBI, A., COLQUITT, D., ROUX, P., GUENNEAU, S. & CRASTER, R.V. 2016 A seismic metamaterial: the resonant metawedge. *Sci. Rep. UK* **6** (1), 27717.

DOLLING, G., ENKRICH, C., WEGENER, M., SOUKOULIS, C.M. & LINDEN, S. 2006 Simultaneous negative phase and group velocity of light in a metamaterial. *Science* **312** (5775), 892–894.

FABBIANE, N., BAGHERI, S. & HENNINGSON, D.S. 2017 Energy efficiency and performance limitations of linear adaptive control for transition delay. *J. Fluid Mech.* **810**, 60–81.

GAD-EL-HAK, M. 1996 Compliant coatings: a decade of progress. *Appl. Mech. Rev.* **49** (10S), S147–S157.

HUSSEIN, M.I., BIRINGEN, S., BILAL, O.R. & KUCALA, A. 2015 Flow stabilization by subsurface phonons. *Proc. R. Soc. Lond. A* **471**, 20140928.

HUSSEIN, M.I., LEAMY, M.J. & RUZZENE, M. 2014 Dynamics of phononic materials and structures: historical origins, recent progress, and future outlook. *Appl. Mech. Rev.* **66** (4), 040802.

HUSSEIN, M.I., ROCA, D., HARRIS, A.R. & KIANFAR, A. 2025 Scatterless interferences: delay of laminar-to-turbulent flow transition by a lattice of subsurface phonons. arXiv:2503.18835

JOUIN, A., ROBINET, J.C. & CHERUBINI, S. 2024 Stability of the flow over superhydrophobic micro roughnesses: the influence of the interface. *Intl J. Thermofluids* **23**, 100707.

KACHANOV, Y.S. 1994 Physical mechanisms of laminar-boundary-layer transition. *Annu. Rev. Fluid Mech.* **26**, 411–482.

KIANFAR, A. & HUSSEIN, M.I. 2023 Phononic-subsurface flow stabilization by subwavelength locally resonant metamaterials. *New J. Phys.* **25** (5), 053021.

KLAUSS, C.W., RUSSO, V., OMRANE, F., HARRIS, A., KIANFAR, A., BREHM, C. & HUSSEIN, M.I. 2025 Control of first and second mode waves in a hypersonic boundary layer flow via phononic subsurface. In *AIAA Aviation Forum and Aascend 2025*. American Institute for Aeronautics and Astronautics.

KOTSONIS, M., SHUKLA, R.K. & PRÖBSTING, S. 2015 Control of natural Tollmien–Schlichting waves using dielectric barrier discharge plasma actuators. *Intl J. Flow Control* **7** (1-2), 37–54.

KRAMER, M.O. 1961 The dophins' secret. *J. Am. Soc. Nav. Engnrs* **73** (1), 103–108.

LANDAHL, M.T. 1962 On the stability of a laminar incompressible boundary layer over a flexible surface. *J. Fluid Mech.* **13** (4), 609–632.

LUCEY, A.D. & CARPENTER, P.W. 1995 Boundary layer instability over compliant walls: comparison between theory and experiment. *Phys. Fluids* **7** (10), 2355–2363.

MICHELIS, T., PUTRANTO, A.B. & KOTSONIS, M. 2023 Attenuation of Tollmien–Schlichting waves using resonating surface-embedded phononic crystals. *Phys. Fluids* **35** (4), 044101.

NAVARRO, J.D., BALDERAS, D., LALONDE, E.J., VELASQUEZ-GONZALEZ, J.C., HOFFMAN, E.N., COMBS, C.S. & RESTREPO, D. 2025 Stabilization of hypersonic shockwave/boundary-layer interactions with phononic metamaterials. *Matter* **8** (7), 102089.

NI, X., WONG, Z.J., MREJEN, M., WANG, Y. & ZHANG, X. 2015 An ultrathin invisibility skin cloak for visible light. *Science* **349** (6254), 1310–1314.

PARK, S., HRISTOV, G., BALASUBRAMANIAN, S., GOZA, A., ANSELL, P.J. & MATLACK, K. 2022 Design and analysis of phononic material for passive flow control. In *AIAA Aviation 2022 Forum*, pp. 3330. American Institute for Aeronautics and Astronautics.

PENDRY, J.B., LUO, Y. & ZHAO, R. 2015 Transforming the optical landscape. *Science* **348** (6234), 521–524.

PENDRY, J.B. & SMITH, D.R. 2006 The quest for the superlens. *Sci. Am.* **295** (1), 60–67.

PFISTER, J.-L. 2019 Instabilities and optimization of elastic strutures interacting with laminar flows. PhD thesis, Université Paris-Saclay, France.

PFISTER, J.-L., FABBIANE, N. & MARQUET, O. 2022 Global stability and resolvent analyses of laminar boundary-layer flow interacting with viscoelastic patches. *J. Fluid Mech.* **937**, A1.

PFISTER, J.-L. & MARQUET, O. 2020 Fluid–structure stability analyses and nonlinear dynamics of flexible splitter plates interacting with a circular cylinder flow. *J. Fluid Mech.* **896**, A24.

PFISTER, J.-L., MARQUET, O. & CARINI, M. 2019 Linear stability analysis of strongly coupled fluid–structure problems with the arbitrary-Lagrangian–Eulerian method. *Comput. Meth. Appl. Mech. Eng.* **355**, 663–689.

PIEST, B.J.T., DRUETTA, P.D. & KRUSHYNSKA, A.O. 2024 Mitigation of flow-induced vibrations in high-speed flows using triply periodic minimal surface structures. *Phys. Fluids* **36** (10), 105119.

ROMAN, J.E., ALVARRUIZ, F., CAMPOS, C., DALCIN, L., JOLIVET, P. & LAMAS DAVIÑA, A. 2023 Improvements to SLEPc in releases 3.14–3.18. *ACM Trans. Math. Softw.* **49** (3), 11.

ROSA, M.I.N., DAVIS, B.L., LIU, L., RUZZENE, M. & HUSSEIN, M.I. 2023 Material vs. structure: topological origins of band-gap truncation resonances in periodic structures. *Phys. Rev. Mater.* **7**, 124201.

SCHLICHTING, H. & GERSTEN, K. 2016 *Boundary-Layer Theory*. Springer.

SCHMID, P.J. & HENNINGSON, D.S. 2001 *Stability and Transition in Shear Flows*. Springer.

SCHMID, P.J., DE PANDO, M.F. & PEAKE, N. 2017 Stability analysis for *n*-periodic arrays of fluid systems. *Phys. Rev. Fluids* **2**, 113902.

SCHURIG, D., MOCK, J.J., JUSTICE, B.J., CUMMER, S.A., PENDRY, J.B., STARR, A.F. & SMITH, D.R. 2006 Metamaterial electromagnetic cloak at microwave frequencies. *Science* **314** (5801), 977–980.

SEMERARO, O., BAGHERI, S., BRANDT, L. & HENNINGSON, D.S. 2013 Transition delay in a boundary layer flow using active control. *J. Fluid Mech.* **731**, 288–311.

SHARMA, A.S., MORRISON, J.F., MCKEON, B.J., LIMEBEER, D.J.N., KOBERG, W.H. & SHERWIN, S.J. 2011 Relaminarisation of $Re_\tau = 100$ channel flow with globally stabilising linear feedback control. *Phys. Fluids* **23** (12), 125105.

SIERRA-AUSIN, J., BONNEFIS, PL, TIRRI, A., FABRE, D. & MAGNAUDET, J. 2022 Dynamics of a gas bubble in a straining flow: deformation, oscillations, self-propulsion. *Phys. Rev. Fluids* **7**, 113603.

SIMON, B., FABBIANE, N., NEMITZ, T., BAGHERI, S., HENNINGSON, D.S. & GRUNDMANN, S. 2016 In-flight active wave cancelation with delayed-x-LMS control algorithm in a laminar boundary layer. *Exp. Fluids* **57**, 160.

SIPP, D. & MARQUET, O. 2013 Characterization of noise amplifiers with global singular modes: the case of the leading-edge flat-plate boundary layer. *Theor. Comput. Fluid Dyn.* **27** (5), 617–635.

SMITH, D.R., PENDRY, J.B. & WILTSHIRE, M.C.K. 2004 Metamaterials and negative refractive index. *Science* **305** (5685), 788–792.

STURZEBECHER, D. & NITSCHE, W. 2003 Active cancellation of Tollmien–Schlichting instabilities on a wing using multi-channel sensor actuator systems. *Intl J. Heat Fluid Flow* **24** (4), 572–583.

TSIGKLIFIS, K. & LUCEY, A.D. 2017 The interaction of Blasius boundary-layer flow with a compliant panel: global, local and transient analyses. *J. Fluid Mech.* **827**, 155–193.

YEO, K.S. 1988 The stability of boundary-layer flow over single-and multi-layer viscoelastic walls. *J. Fluid Mech.* **196**, 359–408.

YEO, K.S. & DOWLING, A.P. 1987 The stability of inviscid flows over passive compliant walls. *J. Fluid Mech.* **183**, 265–292.

ZHANG, R.Z., CONG, Y., SELLAM, M. & CHPOUN, A. 2024 Bandgap analysis of periodic composite plates considering fluid–structure coupling. *J. Sound Vib.* **582**, 118412.

ZHAO, R., LIU, T., WEN, C.-Y., ZHU, J. & CHENG, L. 2019 Impedance-near-zero acoustic metasurface for hypersonic boundary-layer flow stabilization. *Phys. Rev. Appl.* **11**, 044015.

ZIMAN, J.M. 1972 *Principles of the Theory of Solids*, 2nd edn. Cambridge University Press.